Mutation of the α-tubulin Tuba1a leads to straighter microtubules and perturbs neuronal migration

Richard Belvindrah,[1,2,3] Kathiresan Natarajan,[4,5] Preety Shabajee,[1,2,3] Elodie Bruel-Jungerman,[1,2,3] Jennifer Bernard,[1,2,3] Marie Goutierre,[1,2,3] Imane Moutkine,[1,2,3] Xavier H. Jaglin,[6] Mythili Savariradjane,[1,2,3] Theano Irinopoulou,[1,2,3] Jean-Christophe Poncer,[1,2,3] Carsten Janke,[4,5] and Fiona Francis[1,2,3]

[1]Institut National de la Santé et de la Recherche Médicale (INSERM), UMR S-839, Paris, France
[2]Sorbonne Universités, Université Pierre et Marie Curie (UPMC), Université Paris 06, UMR S-839, Paris, France
[3]Institut du Fer à Moulin, Paris, France
[4]Institut Curie, Paris Sciences et Lettres Research Université (PSL), Centre National de la Recherche Scientifique (CNRS), Institut National de la Santé et de la Recherche Médicale (INSERM), UMR 3348, Orsay, France
[5]Université Paris Sud, Université Paris-Saclay, Centre National de la Recherche Scientifique (CNRS), UMR 3348, Orsay, France
[6]Department of Neuroscience and Physiology, Smilow Neuroscience Program, Neuroscience Institute, New York University, New York, NY

Brain development involves extensive migration of neurons. Microtubules (MTs) are key cellular effectors of neuronal displacement that are assembled from α/β-tubulin heterodimers. Mutation of the α-tubulin isotype TUBA1A is associated with cortical malformations in humans. In this study, we provide detailed in vivo and in vitro analyses of Tuba1a mutants. In mice carrying a Tuba1a missense mutation (S140G), neurons accumulate, and glial cells are dispersed along the rostral migratory stream in postnatal and adult brains. Live imaging of Tuba1a-mutant neurons revealed slowed migration and increased neuronal branching, which correlated with directionality alterations and perturbed nucleus–centrosome (N–C) coupling. Tuba1a mutation led to increased straightness of newly polymerized MTs, and structural modeling data suggest a conformational change in the α/β-tubulin heterodimer. We show that Tuba8, another α-tubulin isotype previously associated with cortical malformations, has altered function compared with Tuba1a. Our work shows that Tuba1a plays an essential, noncompensated role in neuronal saltatory migration in vivo and highlights the importance of MT flexibility in N–C coupling and neuronal-branching regulation during neuronal migration.

Introduction

Brain development involves extensive migration of neurons to regions forming the gray matter. Inhibitory neurons or interneurons (INs) are a critical and complex population that regulates resulting brain networks. IN precursors in different brain structures can migrate long distances to reach their appropriate final targets. Embryonic IN precursors destined for the olfactory bulb (OB) originate mainly from the lateral ganglionic eminences (GEs; Corbin et al., 2001) and migrate long distances to arrive at their final position. Continuously, during adult life, new neurons are added in the granular cell layer (GCL) and periglomerular layer of the OB through the rostral migratory stream (RMS), allowing them to become integrated into the preexisting local olfactory circuitry (Lledo et al., 2006; Belvindrah et al., 2009; Lalli, 2014).

This is thought to be important for forming olfactory memories and represents an intensively studied topic. However, the regulation of neurogenesis and migration is not well understood. Cell displacement from regions of production may be an essential step to permit the correct integration and function of these INs.

Neuronal migration to the OB is finely tuned by the synergistic action of cell-extrinsic and -intrinsic cues that contribute to the precise targeting of migrating neurons into the right layer of the OB at the correct time (Chazal et al., 2000; Hack et al., 2002; Murase and Horwitz, 2002; Nguyen-Ba-Charvet et al., 2004; Ng et al., 2005; Kappeler et al., 2006; Koizumi et al., 2006; Belvindrah et al., 2007, 2011; Whitman et al., 2009; Bozoyan et al., 2012; Sonego et al., 2015). There, they differentiate into GABAergic INs according to a well-defined sequence of maturation (Gheusi et al., 2012; Pallotto and Deprez, 2014).

Among the different cytoskeletal components that are crucial for neuronal migration, microtubules (MTs) are thought to support a wide range of functions, such as growth of the leading process

and its dynamic reorientation and coupling of the nucleus with the centrosome during the saltatory movement of neurons (Kapitein and Hoogenraad, 2015; Kawauchi, 2015). In response to extrinsic signals, MTs are extensively remodeled during cell movement. MTs are cytoskeletal fibers that are dynamically assembled from heterodimers made up of evolutionarily conserved α- and β-tubulin subunits. Despite this high degree of conservation, α- and β-tubulins are each coded by multiple genes, several of which are expressed in migrating neurons (Jaglin and Chelly, 2009; Reiner and Sapir, 2009). The study of the specific contribution of each of these tubulin isotypes during migration has so far been challenging, as they exhibit a high degree of homology. Indeed, different tubulin isotypes may be required for specialized MT functions in different cells and compartments (Tischfield and Engle, 2010).

In recent years, the interest in the functional role of tubulin isotypes has strongly increased, as tubulin genes have been found mutated in human cortical malformations that are part of an emerging heterogeneous family known as the tubulinopathies (Bahi-Buisson and Cavallin, 2016; Chakraborti et al., 2016). *Alpha–tubulin 1A* (*TUBA1A*) mutations were among the first identified, leading to lissencephaly with cerebellar hypoplasia, corpus callosum agenesis, and, in rare cases, perisylvian asymmetrical polymicrogyria (Keays et al., 2007; Poirier et al., 2007, 2013; Bahi-Buisson et al., 2008, 2014; Kumar et al., 2010; Fallet-Bianco et al., 2014). Detailed analyses of fetal cases also identified agenesic or dysmorphic OBs (Fallet-Bianco et al., 2008). Thus, Tuba1a is likely to play a critical role in the formation of several brain areas, and its mutation may change the behavior of MTs to an extent that cannot be compensated for by other α-tubulin isotypes expressed in the same cells. Here, we sought to characterize molecular and cellular alterations induced by the S140G mutation of Tuba1a.

We investigated a mouse model with a chemically induced Tuba1a missense mutation and report that this protein plays an important role in neuronal migration in the RMS. This mouse mutant has hippocampal and subtle cortical defects, but abnormalities in the RMS were never previously recognized (Keays et al., 2007). Our data show that the heterozygote S140G mutation is sufficient to produce a strong migratory phenotype in mutant mice, despite the fact that several other α-tubulin genes are also expressed in postmitotic neurons in the affected brain region (Coksaygan et al., 2006). Histological and live-imaging studies using organotypic brain slices revealed a malformed RMS and OB, as well as distinctly altered characteristics of migration. Postnatal subventricular zone (SVZ) electroporations of the same mutation demonstrated impaired nucleus–centrosome (N–C) coupling, directionality, speed, and branching. Using fluorescence imaging and structural-modeling studies, we demonstrate that these alterations are related to functional and structural MT defects. Finally, we demonstrate that Tuba8, another α-tubulin isotype previously associated with cortical malformations (Abdollahi et al., 2009), has altered function compared with Tuba1a, thus highlighting the specificities of these α-tubulins. Our data pinpoint an essential, noncompensated key role of Tuba1a in the RMS, related to tubulin heterodimer structure and to MT integrity, critical in migrating neurons.

Results

RMS and OB alterations in *Tuba1a*-mutant mice

To evaluate the consequences of the Tuba1a S140G mutation during neuronal migration, the RMS was analyzed in sagittal sections from adult control and *Tuba1a*-mutant mice. In contrast to control mice where the RMS appeared as a thin pathway (Fig. 1, A and C), we observed a large accumulation of cells within the RMS of *Tuba1a*-mutant animals (Fig. 1, B and D). The overall organization of the OB was preserved, but its size appeared greatly reduced (Fig. 1 B). In coronal sections, whereas in control mice the RMS remained thin all along the rostral–caudal axis (Fig. 1 E), in *Tuba1a*-mutant mice, a cell accumulation was observed in the central part of the RMS (Fig. 1 F), with a concomitant rostral reduction in the number of cells, clearly visible at the level of the OB. Developmental studies in *Tuba1a*-mutant animals revealed subtle changes in the OB GCL already at embryonic (E16.5; Fig. S3, A and B) and early postnatal stages (Fig. S3, C and D). The RMS develops mainly postnatally (Pencea and Luskin, 2003), and anatomical alterations were clearly visible from P8 onwards (Fig. S3, E–J). Embryonic cortical IN migration streams from the GEs also showed abnormalities in the mutant, with less INs reaching the dorsal telencephalon and hippocampal primordium (Fig. S1, A–G). Measuring RMS thickness in the adult revealed a significant increase in size at two different rostrocaudal levels, RMS2 (75.4 ± 7.2 μm in control vs. 350.8 ± 9.8 μm in mutant mice; P < 0.001; Fig. 1 G) and RMS3 (76.4 ± 12.2 μm in control vs. 269 ± 23.9 μm in mutant mice; P < 0.001; Fig. 1 G). Conversely, the OB surface measured on sagittal sections was smaller in mutant compared with control mice (6.68 ± 0.187 mm^2 in control vs. 5.55 ± 0.119 mm^2 in mutant mice; P < 0.01; Fig. 1 H). Once they reach the OB, neuronal precursors settle mainly in the GCL. We observed a decrease in its surface in mutant mice (3.91 ± 0.147 mm^2 in control vs. 2.51 ± 0.126 mm^2 in mutant mice; P < 0.001; Fig. 1 I). Together, these data show consistent IN migration defects with a severe accumulation of cells in the *Tuba1a*-mutant RMS leading to a reduction of OB size related to the GCL in the mutant brain.

We further characterized the identity of cells that accumulate in the RMS. Staining with the neuronal anti–PSA-NCAM (polysialylated neural cell adhesion molecule) antibody revealed a normal thin stream in control mice (Fig. 2, A–C) but an abundance of PSA-NCAM–positive (PSA-NCAM^{+}) cells in the core of the mutant RMS (Fig. 2, D–F). At higher magnification, PSA-NCAM^{+} neurons were observed to form chains of cells in the control RMS (Fig. 2 C, and Fig. S3, K–N) but appeared more numerous and less directional in the mutant RMS2 region (Fig. 2 F) and unchanged in the RMS1 region (Fig. S3, K–N). Neurons in chains migrate within glial corridors (Lois and Alvarez-Buylla, 1994; Doetsch and Alvarez-Buylla, 1996; Wichterle et al., 1997; Kaneko et al., 2010). When comparing these glial structures by glial fibrillary acidic protein (GFAP) staining, we observed a corresponding increase in the size of the astrocytic tunnels that surround the clusters of neurons in adult mutant animals (Fig. 2, G–J). Glial defects were less obvious at early postnatal (P8) stages (Fig. S2, A–D), despite the neuronal accumulation. We estimated the density of GFAP[+] glial fibers in the RMS of adult control and mutant mice and observed a significant decrease in the RMS1 region and similar tendencies in RMS2 and RMS3 (Fig. S2, E–K). Thus, the increase in size of the GFAP[+] region is partially compensated by a decrease of fiber density, and larger dispersions of GFAP[+] fibers are observed in mutant caudal regions.

Furthermore, most cells migrating toward the OB are transiently present in the RMS and do not differentiate along its
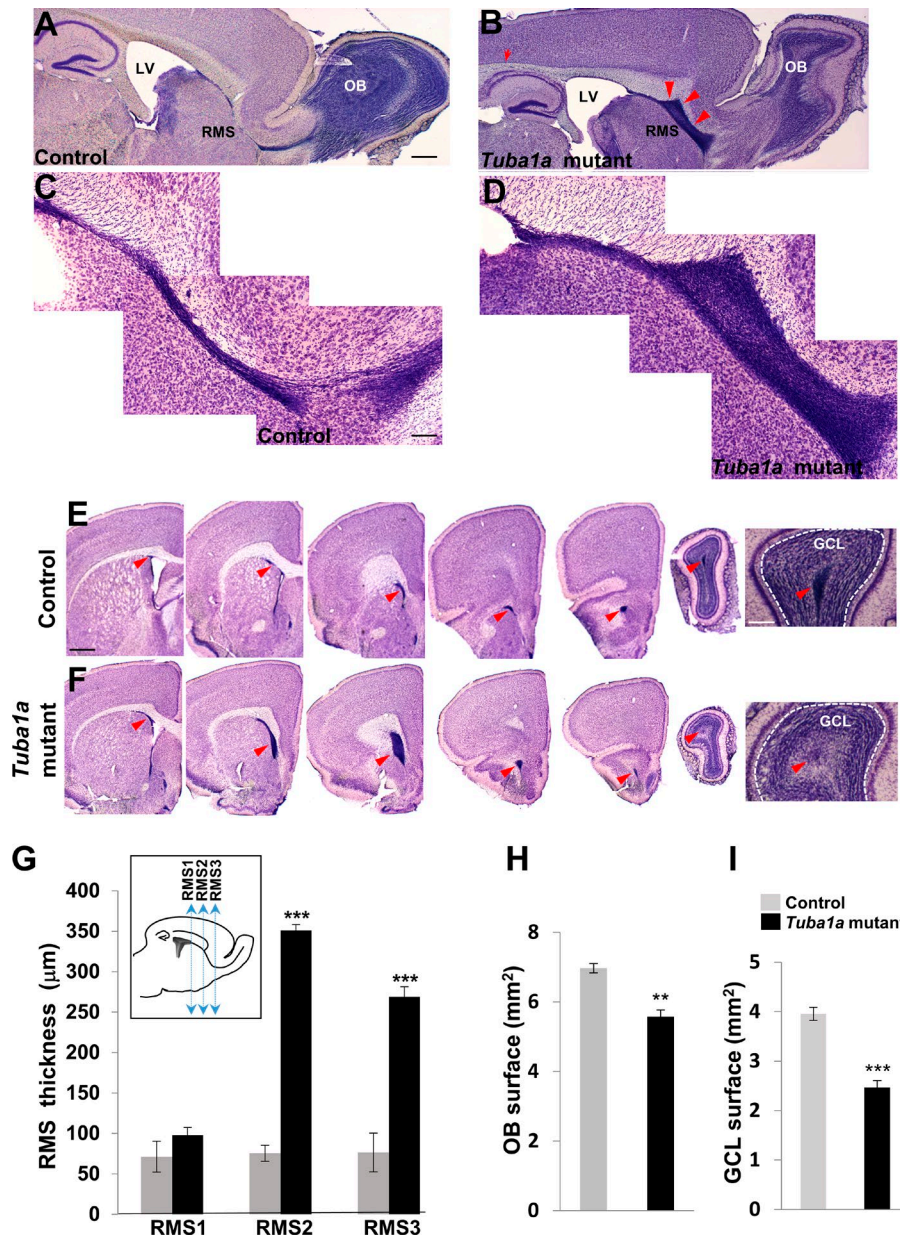
Figure 1. **Alteration of the RMS in adult** ***Tuba1a*-mutant mice.** (A and B) Low-magnification image of sagittal brain sections after Nissl staining in control (A) and mutant (B) brains. Note that the RMS is enlarged in the *Tuba1a*-mutant brain (red arrowheads). (C and D) Higher magnification of the RMS in the sagittal view is shown in control (C) and *Tuba1a*-mutant (D) brains, revealing an increase in RMS size in the mutant brain. (E and F) Low-magnification image of coronal brain sections after Nissl staining in control (E) and mutant (F) brains. Note that the RMS is enlarged in the mutant condition (F) at different rostral levels, and OB neurons are reduced. The GCL is outlined with white dashed lines. Arrowheads indicate the RMS. (G) RMS thickness was measured at three different rostrocaudal levels (RMS1, RMS2, and RMS3 according to the schema). Note the increased thickness of mutant RMS2 and RMS3. (H) The overall OB surface was measured in control and *Tuba1a*-mutant brains. Note the decreased OB size in the mutant. (I) The GCL surface was measured in control and *Tuba1a*-mutant brains. Note the decreased surface in the mutant. (G–I) **, P < 0.01; ***, P < 0.001. *n* = 5. Data are represented as mean ± SEM. LV, lateral ventricle. Bars: (A) 437 µm; (C) 87 µm; (E) 650 µm; (E and F, right) 175 µm.

path (Luskin, 1993; Lois and Alvarez-Buylla, 1994; Jankovski and Sotelo, 1996). Whereas migrating neurons in control brains rarely express calretinin, a marker of IN differentiation, many calretinin+ cells were found in the mutant RMS (Fig. 2, K–M). The numbers of calretinin+ cells were quantified at four different rostrocaudal levels (RMS1, RMS2, RMS3, and RMS4; Fig. 2 N), and a tendency of decreasing densities from RMS1–4 was observed in control brains. At the RMS2 level, a significant increase of calretinin+ cells was observed in the *Tuba1a* mutant (37.33 ± 10.6 cells in control vs. 171.91 ± 24.95 cells in mutant mice; P < 0.001; Fig. 2 N). This suggests that slowed or blocked neurons in the RMS are able to continue an intrinsic program of maturation.

Electroporation of the S140G mutation reduces SVZ-derived GFP+ cells migrating to the OB

To test whether the defect observed in the *Tuba1a*-mutant RMS is cell autonomous, we electroporated the SVZ of P0–P2 WT

mice with a construct expressing either GFP alone or GFP and the Tuba1a protein, with or without the S140G mutation, under the control of the *doublecortin* (*Dcx*) promoter (Fig. 3 G). This allowed us to test the expression of WT or mutant α-tubulin in GFP+ migrating neurons. The majority of cells electroporated with GFP only or with the WT Tuba1a construct migrated along the RMS and reached the OB (Fig. 3, A, B, D, and E), indicating no obvious effect of WT Tuba1a overexpression. On the contrary, the S140G mutation led to less GFP+ neurons reaching the OB and more retained at the beginning of the RMS (Fig. 3, C and F). Automated counting of GFP+ cells per region (Fig. 3 H, SVZ, RMS, and OB) showed that those expressing S140G were significantly increased in the SVZ and the RMS and reduced in the OB in comparison with the control constructs (Fig. 3 H). Together, these data show that a cell-autonomous defect of the S140G mutation leads to a phenotype in migrating neurons. Glial fibers in early electroporated brains resembled WT (Fig. S2, L and M), although glial defects that accumulate over time cannot be excluded in this model.
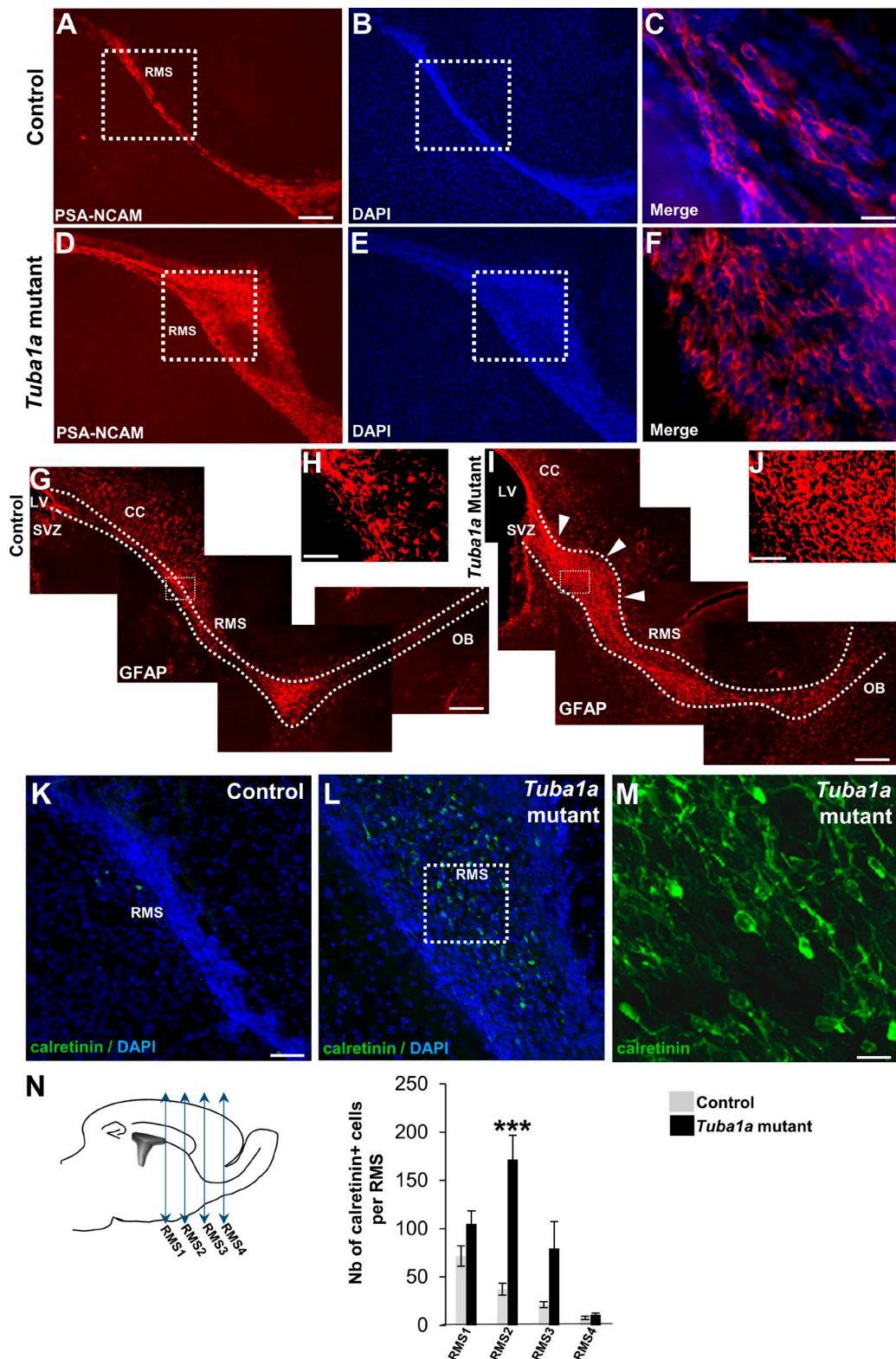
Figure 2. **PSA-NCAM+ migrating neuron, GFAP+ glial fiber, and calretinin+ neuron differentiation defects in the mutant RMS.** (A–F) Immunostaining of PSA-NCAM on sagittal sections (A and D) and counterstaining with DAPI (B and E) revealed a thin RMS in the control brain (A) compared with an enlarged RMS in the mutant (D). (C and F) Higher magnification of PSA-NCAM and DAPI staining in the regions outlined in B and E, respectively. Note the existence of PSA-NCAM+ neurons migrating in organized chains in the control brain (C), whereas in the region of accumulation of neurons in the mutant, the PSA-NCAM+ cells are more numerous and appear less organized (F). (G and I) Low-magnification images of GFAP immunostaining on sagittal sections in control and mutant brains. The RMS is outlined with dashed lines. A meshwork of GFAP+ fibers associated with the stream was observed in the control RMS (G), whereas in the mutant, the GFAP+ glial fibers cover a larger region where the accumulation of neurons is observed (I). Arrowheads indicate regions of dramatically enlarged GFAP staining. (H and J) Higher magnification of GFAP staining in the regions outlined in G and I, respectively. Note the existence of disorganized glial fibers in the mutant (J) compared with the control (H). (K–N) Calretinin immunostaining
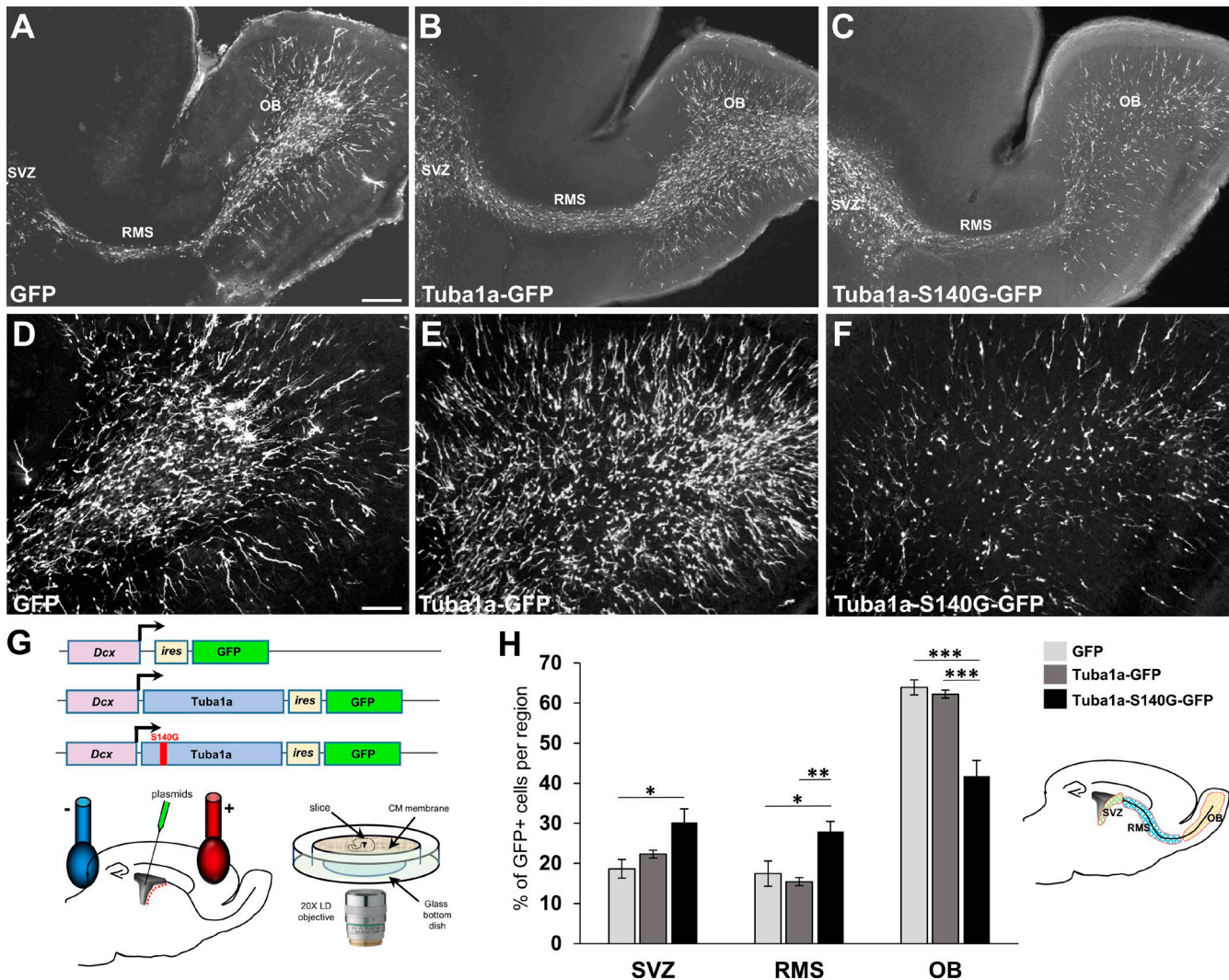
Figure 3. **Expression of a Tuba1a S140G-mutant construct by electroporation in P0–P2 mouse pups impairs neuronal migration in the RMS.** (A–C) Low-magnification images of GFP staining on sagittal brain sections after electroporation of GFP only (A), control WT Tuba1a (B), or Tuba1a S140G-mutant (C) ires GFP constructs at 5 dpe. (D–F) Higher magnifications of the OB are represented. Note the decreased number of GFP+ neurons in the OB from the brain electroporated with the mutant S140G construct. (G) Description of the three constructs used in this study: GFP only, control Tuba1a, and Tuba1a S140G constructs with GFP separated by an ires. The *Dcx* promoter controls expression. Schemas of the electroporation as well as the live-imaging system for slices from electroporated brains are shown. (H) Quantification of the percentage of GFP+ neurons per region (SVZ, RMS, and OB, as indicated in the schema) for GFP only, control Tuba1a, and Tuba1a S140G-mutant conditions. No significant differences were observed between GFP only and control Tuba1a conditions. Note the increase in the percentage of GFP+ neurons in the SVZ and the RMS but decrease in the OB for the S140G-mutant construct. *, $P < 0.05$; **, $P < 0.01$; ***, $P < 0.001$. $n = 4$–5. Data are represented as mean ± SEM. Bars: (A) 248 μm; (C) 64 μm.

The Tuba1a S140G mutation alters the speed, directionality, and branching of migrating neurons

To study more precisely the neuronal migration defects generated by the S140G mutation, WT mice were again electroporated with either Tuba1a WT or S140G-mutant constructs (as no difference was observed between GFP alone and Tuba1a WT-GFP previously). We analyzed migration in the RMS 5 d post-electroporation (dpe) by live imaging with a spinning-disk microscope. Control Tuba1a GFP+ cells migrated tangentially along the RMS within the normal stream (Fig. 4, A and C; and Video 1). Neurons expressing the S140G mutation migrated less uniformly, no longer parallel and unidirectional within the main stream as in the control (Fig. 4, B and D; and Video 2). In both conditions, individual neurons were numbered and tracked as shown in the displayed sequences (Fig. 4, A–D). The speed of migration as well as directionality and branching were quantified from time-lapse videos.

counterstained with DAPI in the RMS on sagittal brain sections from control (K) and mutant (L) brains. Note that, in the control brain, few calretinin+ cells were observed, whereas in the mutant brain, numerous calretinin+ cells were present in the RMS2 region. (M) An enlargement of the region outlined in L. Calretinin+ cells present complex morphologies. (N) Calretinin+ cells were quantified at four different levels of the RMS. Note the increase in the number (Nb) of calretinin+ neurons in mutant RMS2. ***, $P < 0.001$. $n = 5$. Data are represented as mean ± SEM. CC, corpus callosum; LV, lateral ventricle. Bars: (A) 140 μm; (C) 24 μm; (G) 210 μm; (H) 45 μm; (I) 210 μm; (J) 45 μm; (K) 60 μm; (M) 12 μm.
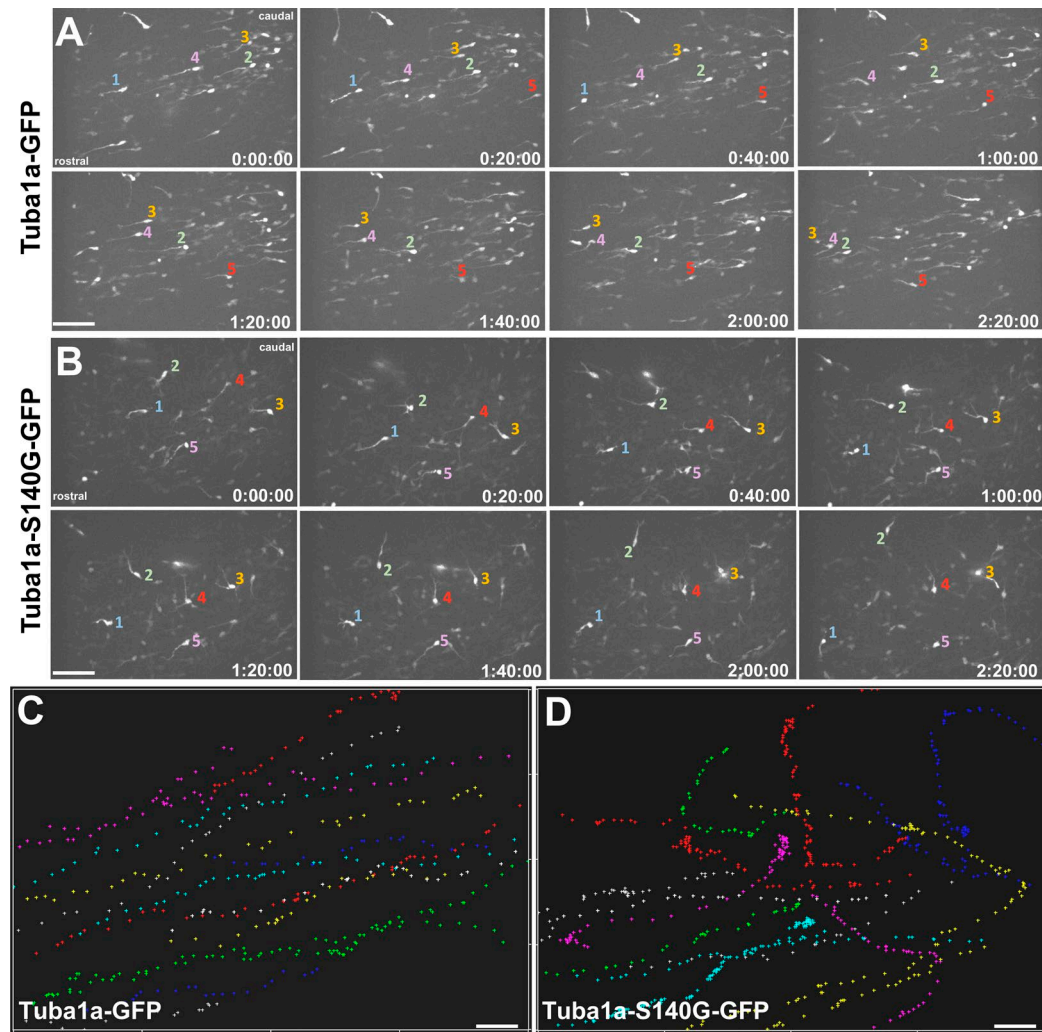
Figure 4. **Impaired directionality after electroporation with the Tuba1a S140G-mutant construct.** (A and B) Time-lapse video microscopy sequences for control Tuba1a (A) or S140G-mutant (B) constructs. An example of tracking for five different neurons is shown (numbered in color from one to five) within a video frame of 2 h 20 min (every 20 min) for both conditions. Rostrocaudal orientations are indicated in the first image of each sequence. Neurons migrated mainly tangentially along the RMS in the Tuba1a control condition (A), whereas with the Tuba1a S140G-mutant construct, the migration appeared less organized, showing more frequent changes of direction. (C and D) An example of the tracking of 15 neurons is shown in Tuba1a control (C) and Tuba1a S140G-mutant (D) conditions. Neurons migrated less unidirectionally after electroporation with the Tuba1a S140G-mutant construct. Bars: (A and B) 56 µm; (C and D) 26 µm.

First, we quantified mean migration speed by tracking and performing instantaneous speed measurements. A significant decrease in the mean speed was observed for S140G-mutant neurons (90.3 ± 2.79 µm/h for control vs. 74.4 ± 2.14 µm/h for mutant; P < 0.001; Fig. 5 A). Similar defects in cortical IN migration speed were also observed in E12.5 GE explant cultures from WT and *Tuba1a*-mutant brains (Fig. S1 G). In the RMS, Tuba1a S140G-electroporated neurons showed abnormal directionality (Fig. 4, C and D). This was quantified by plotting each cell according to their angles deviating from the rostral direction, comparing positions at the beginning to the end of the sequence. Whereas a high proportion of control neurons (54%) migrate rostral and tangential to the stream (at 270°, rostral; Fig. 5 B), only 22% of the mutant neurons do this (Fig. 5 B, P < 0.001). Many Tuba1a S140G neurons migrated oblique and perpendicular to the stream and even backward (Fig. 5 B), confirming the initial observation of the more randomized migration direction in the mutant condition (Video 2).

Analysis of WT neuron migration speed distributions revealed a potential bimodal distribution. This was assessed using Hartigan's dip test (P < 0.01) together with the Akaike Information Criterion (AIC). The experimental data fitted with a Gaussian mixture model revealing two Gaussian curves (Fig. 5 C). The threshold between the two classes of migrating neurons was mathematically defined as the intersection between the two curves, occurring at 75.4 µm/h. We termed these slow (<75.4 µm/h) and fast (>75.4 µm/h) migrating cells (Fig. 5 C). As speed of migration has been associated with complexity of neuronal branching (James et al., 2011), individual neurons exhibiting fast and slow speeds were then classified according to four different categories, depending on the number of processes they exhibited during migration (one, two, three, or four processes; Fig. 5 D). Among control neurons, no significant difference in categories was observed between fast and slow migrating neurons (Fig. 5 E). For the mutant, we observed a modest but significant difference within categories 1 (slow migration, 70.3 ± 3.3% of neurons vs. fast migration, 79.3 ± 3.1% of neurons,
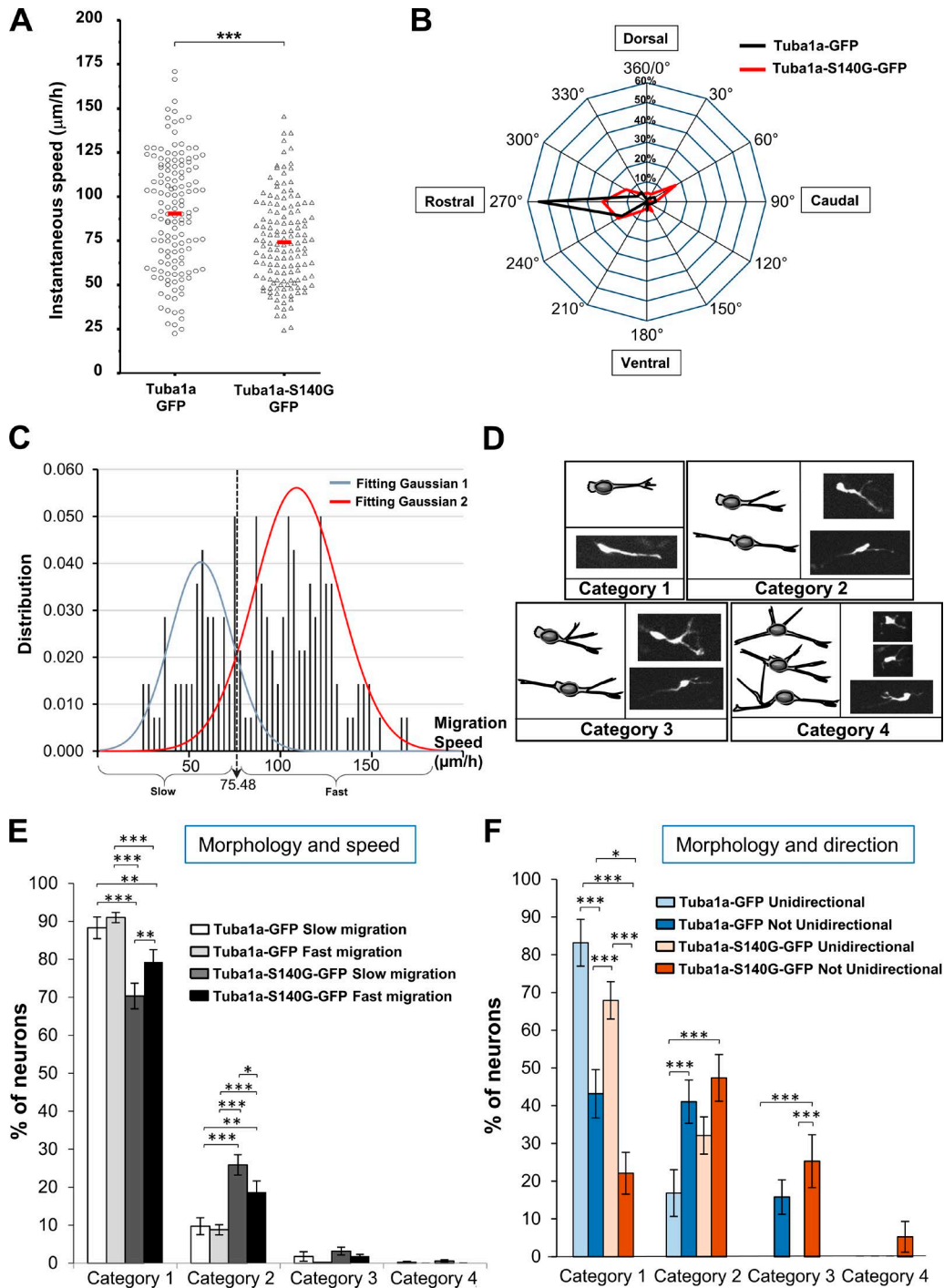
Figure 5. **Speed, directionality, and branching defects after electroporation of the Tuba1a S140G-mutant construct.** (A) Time-lapse video films were analyzed from control and S140G-mutant conditions, and mean instantaneous speeds were determined (short red line). Note the decrease in the mean speed of migration at 5 dpe with the mutant S140G construct. *n* = 140 cells per group from three independent experiments. (B) Quantification of directionality of migration: each cell was plotted according to the angle formed from the location at the beginning to the end of the migratory sequence (from 0 to 360° with 0°/360° being dorsal, 90° caudal, 180° ventral, and 270° rostral). Note the significant decrease in the percentage of neurons migrating tangentially and rostrally toward the OB after electroporation with the Tuba1a mutant S140G construct. *n* = 90 cells per group from three independent experiments. (C) The density of distribution for control Tuba1a instantaneous speed measurements was determined. The analysis revealed a bimodal distribution validated with Hartigan's dip test (P < 0.01) and the AIC. *n* = 140 cells from control condition from three independent experiments. The threshold speed between fast- and slow-migrating neurons was defined mathematically at 75.48 µm/h. (D) Description of the four different categories of branching morphology used for the quantifications in E and F. Each category corresponds to a level of complexity of the migrating neurons with one, two, three, or four processes. (E) Among control Tuba1a neurons, no significant difference in category between fast and slow migration was observed (white and light gray bars). For Tuba1a S140G, less category 1 and more category 2 neurons were observed for both fast and slow migration (dark gray and black bars). Slow migrating mutant neurons (dark gray) showed even less category 1 and more category 2 neurons. *n* = 90 cells per group. Data are represented as mean ± SEM. (F) For control and mutant Tuba1a non-unidirectional neurons, a strong decrease of category 1 was observed concomitantly with an increase of category 2. For the mutant Tuba1a S140G neurons (salmon and orange bars specifically), the decrease of category 1 non-unidirectional neurons was

P < 0.01; Fig. 5 E) and 2 (slow migration, 25.8 ± 2.6% of neurons vs. fast migration, 18.7 ± 2.9% of neurons, P < 0.05; Fig. 5 E). Indeed, slow mutant neurons are more complex than fast mutant neurons, and mutant neurons, in general, are more complex than control neurons.

We also correlated morphology with directionality (uni-directional vs. non-unidirectional). Comparing even control migrating neurons between them revealed a significant decrease of category 1 (unidirectional, 83.1 ± 6.2% of neurons vs. non-unidirectional, 43.1 ± 6.4% of neurons, P < 0.001; Fig. 5 F) and increase of category 2 (unidirectional, 16.8 ± 6.2% of neurons vs. non-unidirectional, 41 ± 5.7% of neurons, P < 0.001; Fig. 5 F) neurons related to non-unidirectionality. Hence, less directionality is associated with increased branching complexity. Comparatively, in the mutant, the same trends were observed; significantly decreased non-unidirectional category 1 neurons (unidirectional, 67.8 ± 4.9% of neurons vs. non-unidirectional, 22.1 ± 5.5% of neurons, P < 0.001; Fig. 5 F) were replaced by higher complexity neurons (category 2: unidirectional, 32.1 ± 4.9% of neurons vs. non-unidirectional, 47.3 ± 6.2% of neurons, NS; category 3: unidirectional, 0% of neurons vs. non-unidirectional, 25.2 ± 7% of neurons, P < 0.001; Fig. 5 F). Thus, mutant neurons show increased complexity associated with abnormal directionality. Abnormal neuronal complexity and directionality hence strongly contribute to the *Tuba1a*-mutant RMS phenotype. Further analyses (unpublished data) revealed that abnormal new branches can occur either from the soma or from the leading process with no differences between the genotypes.

N–C coupling is altered during saltatory migration of Tuba1a S140G-mutant neurons

The cyclic repetition of elongation of the leading process, followed by nucleokinesis and retraction of the trailing process, generates a global forward progression of the neuron. Nucleokinesis in migrating INs depends strongly on synchronization with forward movement of the centrosome (Fig. 6 B; Tanaka et al., 2004; Bellion et al., 2005). To more precisely track the movement of the centrosome relative to the nucleus (measured from soma position), the distance separating these two organelles was assessed. For this, a PACT-mKO1 centrosome targeting vector was coelectroporated with Tuba1a WT and S140G-mutant constructs to label the centrosome with monomeric Kusabira Orange (mKO1) fluorescent protein. This allowed visualization of centrosome displacement during the migration cycle. Videos showed that, at the beginning of the cycle, the centrosome is very close to the soma and then progressively moves forward with the extension of the leading process (Fig. 6 A and Video 3). To complete neuronal movement, in most cases, the nucleus rejoins the centrosome followed by the advancement of the trailing process. Hence, migration is composed of the cyclic repetition of the separation and recoupling of the nucleus and the centrosome (Fig. 6 B). The oscillating cycle time and the distance between the edge of the soma and the centrosome were measured (Fig. 6 C and Videos 3 and 4).

The automatized analysis of WT and mutant cells revealed a significant increase in the mean duration of the saltatory cycle (14.1 ± 0.39 min for control vs. 15.9 ± 0.53 min for the S140G-mutant construct; P < 0.01; Fig. 6 D) and in the maximum distance coupling the nucleus and the centrosome in the S140G-mutant condition (10.3 ± 0.44 μm for control vs. 12.3 ± 0.67 μm for the S140G-mutant construct; P < 0.01; Fig. 6 E). In most WT migrating neurons, a forward recoupling of the nucleus was observed, with only in rare cases a reversal of centrosome movement (Fig. 6 F and Videos 3 and 4). A significant increase of events when the centrosome moved backward to rejoin the nucleus was observed in mutant cells (3.2% for control vs. 11.4% for the S140G-mutant construct; P < 0.05; Fig. 6 G). This observation, as well as the N–C distance, and the increased duration of the saltatory cycle indicate substantial perturbations in somatic regions likely to contribute to abnormal migration speed and directionality in the Tuba1a S140G-mutant condition.

MT polymerization characteristics with Tuba1a WT, S140G mutation, and Tuba8 WT overexpression

To identify MT defects potentially contributing to these cell phenotypes, Neuro-2a cells were differentiated and transfected with an end-binding 3 (EB3)–mCherry construct to track the plus ends of MTs during ongoing polymerization. MT polymerization dynamics were first monitored in the presence of Tuba1a WT or S140G constructs and then compared with experiments in which Tuba8 WT alone or in the presence of Tuba1a S140G was expressed in these cells. We wished to test whether Tuba8 could rescue the effects of the Tuba1a S140G mutation when present in the same cells.

We analyzed two parameters: MT polymerization speed and MT straightness (Fig. 7, A–E; and Videos 5–8). Both parameters were measured independently in the soma and in the neuritic processes. In the soma, the Tuba1a S140G mutation lead to increased polymerization straightness in comparison with control Tuba1a (Fig. 7 B and Table S1), whereas polymerization speed was not significantly altered (Fig. 7, C and E). Strikingly, Tuba8 led to an MT behavior that differed from both control and mutant Tuba1a in both the soma and the process, reducing straightness and increasing polymerization speed (Fig. 7, B–E). Similarly, the combination of Tuba8 and Tuba1a S140G led to significantly different MT dynamics compared with Tuba1a S140G alone (Fig. 7, B–E). Indeed, coexpression had a similar effect to Tuba8 overexpression alone. Thus, in most conditions tested, Tuba8 overexpression overrides the effects of Tuba1a when it is present in the same cell (Fig. 7 E). These results suggest functional specificities of Tuba1a versus Tuba8 related to their capacities of modulating dynamic parameters during MT polymerization.

These data also demonstrate that the Tuba1a S140G mutation has functional consequences on growing MTs. The specific effects on straightness might contribute to alterations in N–C coupling, as well as to increased branching. These defects are likely to affect the overall efficiency in speed and direction of neuronal migration.

---

associated with an increase of category 2, 3, and 4 neurons. Note that increased morphological complexity is associated with lack of directionality in both control and mutant conditions; however, mutant neurons show higher complexities. n = 100 cells per group. Data are represented as mean ± SEM. *, P < 0.05; **, P < 0.01; ***, P < 0.001.
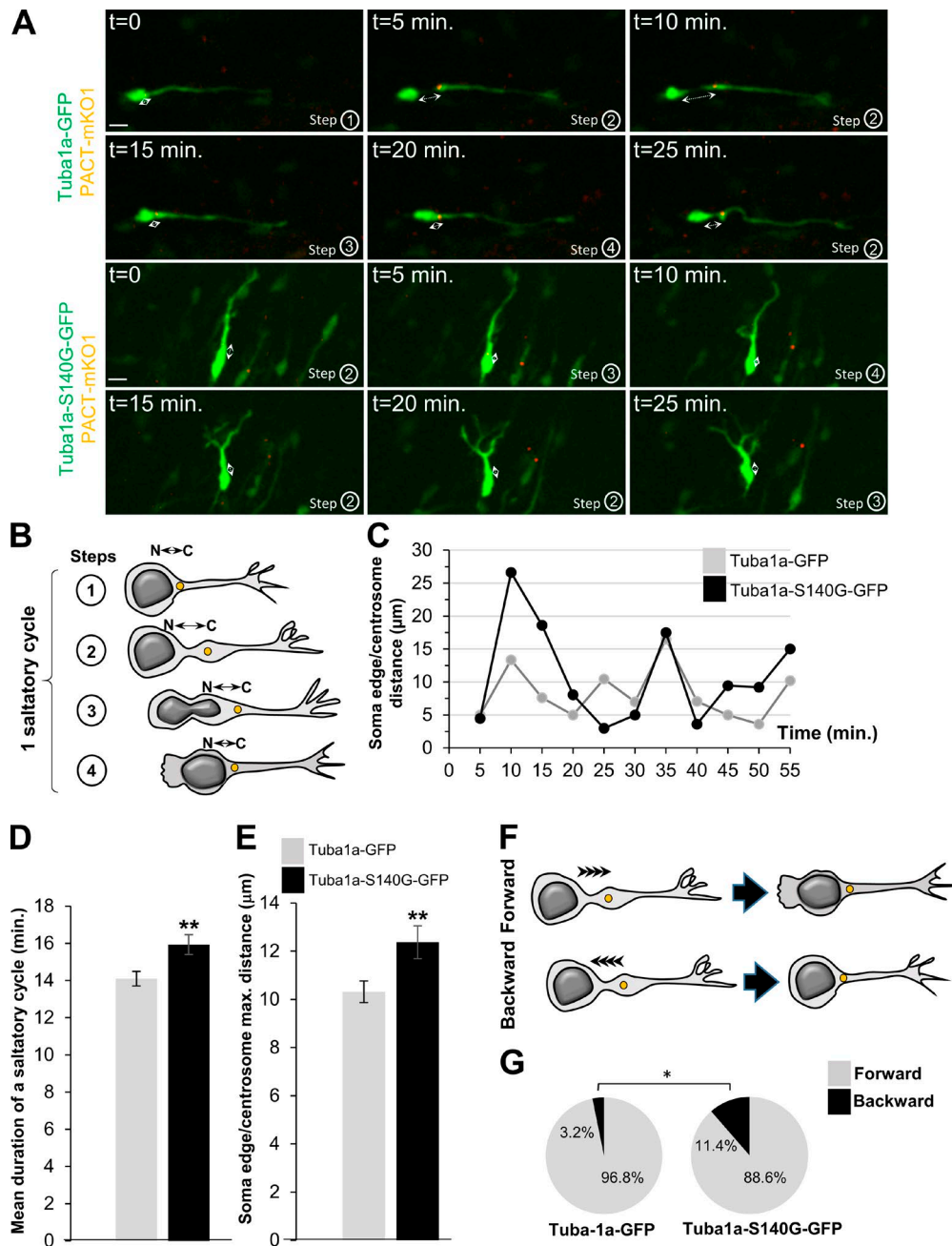
Figure 6. **Expression of the Tuba1a S140G-mutant construct impairs N–C coupling during neuronal migration.** (A) Example of a time-lapse video microscopy sequence with acquisition frames each 5 min showing a GFP-positive neuron expressing PACT-mKO1 (orange fluorescence) located at the centrosome together with either the control (top) or S140G-mutant (bottom) Tuba1a. The corresponding phase of the saltatory cycle step is noted, as also schematized in B. The distance between the edge of the soma and the centrosome was measured in each time frame as indicated with the double arrow and dashed line. Bars, 13 μm. (B) Schematic representation of the forward progression of the centrosome during one saltatory cycle. Note that this distance is minimal at the beginning of a saltatory cycle, becomes maximal when the centrosome moves forward in the swelling, and then returns to minimum when the nucleus rejoins the centrosome. (C) Representative examples of soma edge/centrosome distance oscillations in Tuba1a-GFP and Tuba1a-S140G-GFP neurons. Durations of saltatory cycles and soma edge/centrosome maximum distances were automatically extracted from these oscillations with a Matlab script. n = 93 cells for control and n = 79 cells for mutant from three independent experiments. (D) The mean duration of a cycle of soma edge–centrosome coupling is significantly increased with the Tuba1a S140G-mutant construct. n = 93 cells for control and n = 79 cells for mutant. Data are represented as mean ± SEM. (E) The maximum distance between the soma edge and centrosome was increased with the Tuba1a S140G-mutant construct. n = 93 cells for control and n = 79 cells for mutant from three independent experiments. Data are represented as mean ± SEM. (F) Schematic representation of two examples at the completion of the saltatory cycle: either the nucleus moves forward toward the centrosome (forward class) or the centrosome moves backward toward the nucleus (backward class). (G) Increased percentage of the backward population among the mutant neurons and decreased percentage of forward class. *, P < 0.05; **, P < 0.01. n = 30 cells for control and n = 40 cells for mutant from three independent experiments.
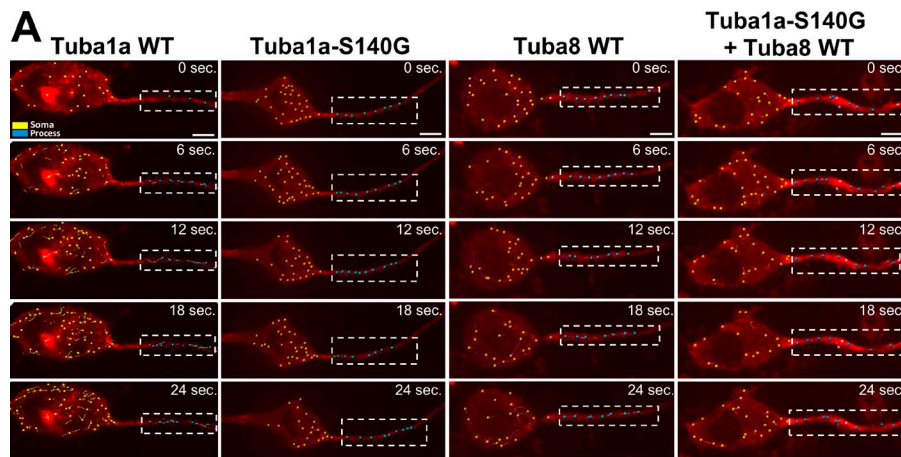
Figure 7. **MT dynamic defects after expression of the Tuba1a S140G-mutant construct.** (A) Example of a 24-s time-lapse video microscopy sequence of EB3-mCherry tracking in Neuro-2a cells after transfection with control WT Tuba1a, mutant Tuba1a S140G, control WT Tuba8, and combined Tuba1a S140G + Tuba8 WT. The EB3-mCherry spots were tracked every 6 s in two different cellular compartments: in the soma (yellow dots) and in the process (blue dots in the outlined rectangle). Bars, 6.4 µm. (B–E) EB3-mCherry polymerization (polym.) straightness (B and D) is significantly increased in the soma of cells expressing the mutant Tuba1a S140G construct (B, first two bars). EB3-mCherry polymerization speed is not changed with the mutant Tuba1a S140G construct in either the soma or process (C and E). Comparatively, control Tuba8 overexpression decreased EB3-mCherry polymerization straightness both in the soma and the process (B and D) and increased the EB3-mCherry polymerization speed in the soma (C and E). Coexpression of mutant Tuba1a S140G together with Tuba8 did not restore the EB3-mCherry polymerization straightness nor the speed to the control level and gave results similar to Tuba8 alone. *, P < 0.05; ***, P < 0.001. n = 8,253 spots for control Tuba1a; n = 8,933 spots for Tuba1a S140G mutant; n = 8,450 spots for control Tuba8; n = 9,182 for Tuba1a S140G mutant + Tuba8 in the soma; n = 2,185 spots for control Tuba1a; n = 1,450 spots for Tuba1a S140G mutant; n = 2,242 spots for control Tuba8; and n = 3,065 for Tuba1a S140G mutant + Tuba8 in the processes. Data are represented as mean ± SEM.
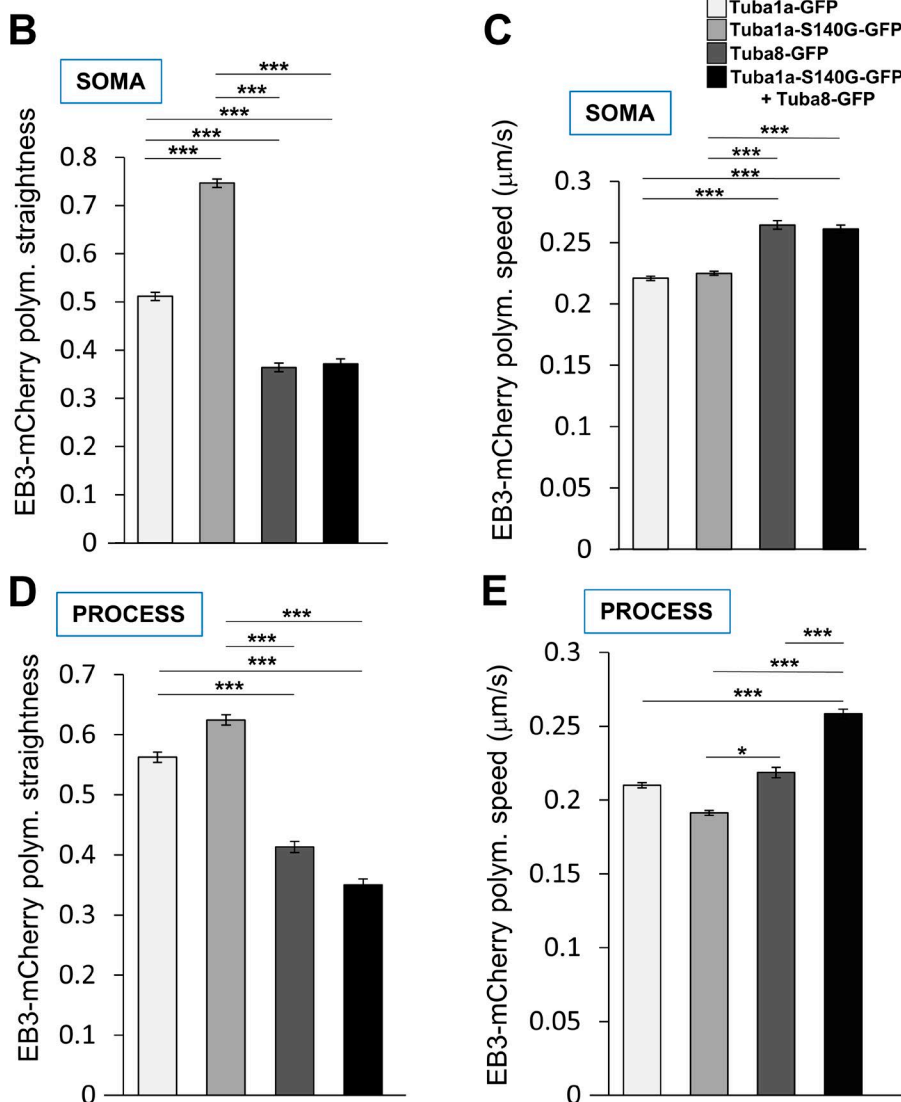
Tubulin heterodimer structure and dynamics are altered between tubulin isotypes and with specific mutations

We further explored the impact of the mutation on the structure of the tubulin heterodimer by structural modeling and molecular dynamics simulations (Fig. 8, A–E; and Figs. S4 and S5). In our dynamics simulation, the time-dependent changes in values of root-mean-square deviation (RMSD) of α- and β-tubulin subunits in WT and mutant dimers indicated that mutant α-tubulin, more so than β-tubulin, undergoes structural changes compared with WT (Fig. S4, A and B). Root-mean-square fluctuations (RMSFs) calculate the flexibility of different regions in the protein: those that are highly flexible show a larger RMSF value, whereas those that are rigid show a lower RMSF value. We ob-
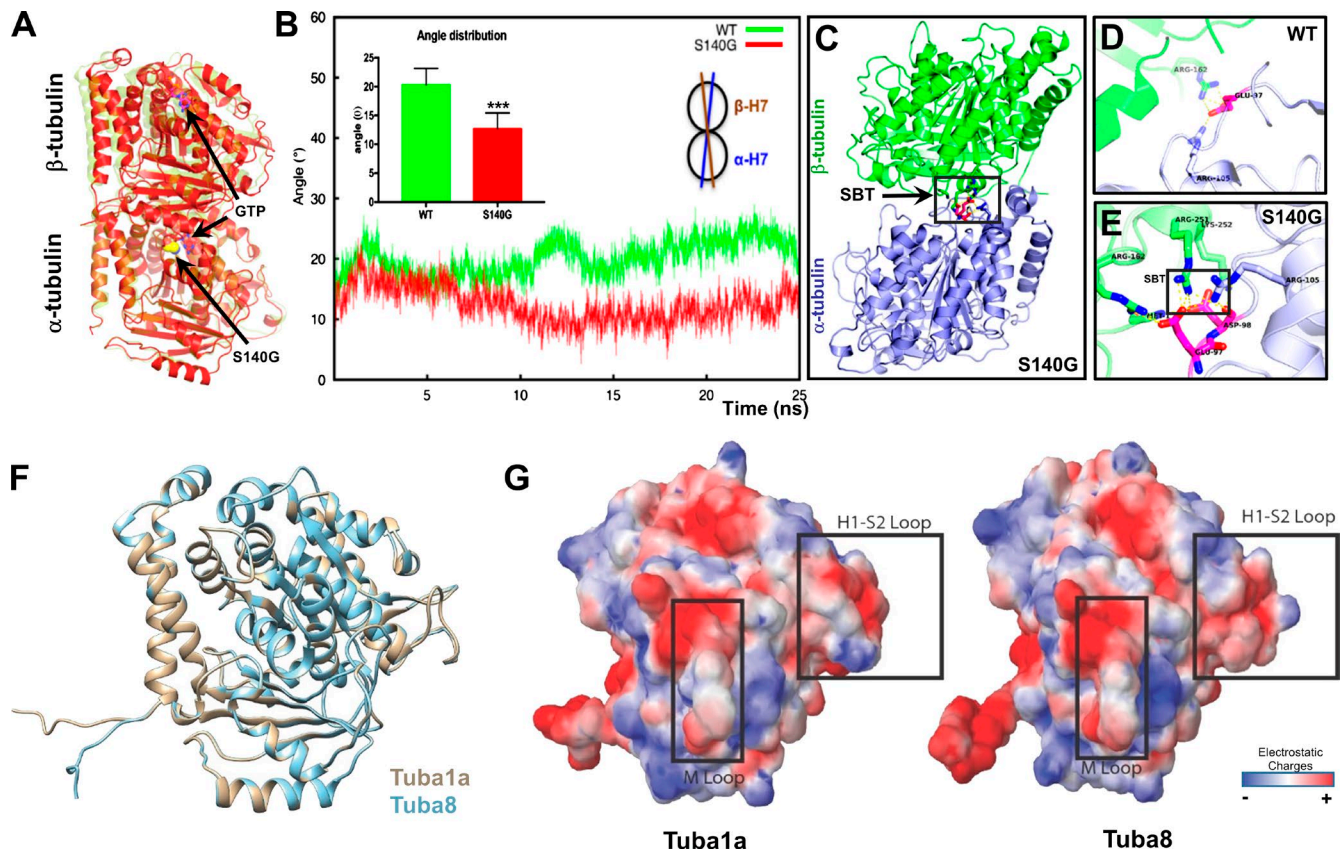
Figure 8. **Structural comparisons between Tuba1a, Tuba1a S140G, and Tuba8.** (A) Structural superposition of time-averaged tubulin structures from WT (light green) and S140G-mutant (red) simulations. The S140G mutation is shown as well as the GTP binding sites. (B) Time evolution of intradimer angle between α-core helix H7 and β-core helix H7 in WT (green) and S140G mutant (red). The inset shows a lower angle distribution in the mutant than in WT, indicating straighter dimers for the mutant tubulin dimer. ***, $P < 0.001$. Data are represented as mean ± SEM. A total of 6,250 points was used. (C) The S140G mutant forms an additional salt-bridge triad (SBT) buried at the intradimer interface (highlighted in box). The α-tubulin is colored in blue, and β-tubulin is in green. (D and E) Higher magnification of intradimer interface for WT and S140G-mutant tubulin. The salt-bridge triad in the S140G mutant (highlighted in box) involves α:Asp98 with β:Arg162 and β:Arg251. The α:Asp98–β:Arg251 interaction is absent in WT. (F) Structural model superposition of Tuba1a (brown) and Tuba8 (light blue) revealed slight differences. (G) Electrostatic analysis of Tuba1a and Tuba8. The H1-S2 loop cooperates with the M loop from adjacent protofilaments. Whereas Tuba1a presents cooperative positive charges in the H1-S2 loop, Tuba8 presents a more negative charge distribution.

served that the mutant shows slower dynamics in several important structural elements known to be involved in lateral and longitudinal MT contacts along the lattice compared with the WT protein (Fig. S4, C and D). Thus, the incorporation of mutant tubulin dimers is likely to induce changes in MT dynamics.

Simulations further showed that mutant S140G induces a straighter conformation of dimers compared with WT, which adapts a slightly curved conformation in the nonpolymerized state. Fig. 8 A shows the superposition of time-averaged structures of WT (green) and S140G-mutant (red) proteins and shows a deviation between mutant and WT tubulin dimers. To further characterize their conformational flexibility, the intradimer angles subtended by the axes of α-core helix H7 and β-core helix H7 were computed. The resulting time-dependent angle changes between WT and mutant are shown in Fig. 8 B. The inset shows the probability of computed angular distributions over 25-ns simulations. The distribution is nearly Gaussian, showing a peak at an angle of ~22° for WT and ~12° for the S140G mutant ($P < 0.001$). The angle values indicate that the S140G mutant restricts the conformational flexibility of the tubulin dimer and favors a straighter conformation compared with WT.

We further analyzed the mode of GTP interactions in Tuba1a WT (Fig. S5 A) and S140G mutant (Fig. S5 B). In WT

heterodimers, S140, which is close to the GTP-binding site, stabilizes GTP in the active site by forming hydrogen bonds. In contrast, in the S140G mutant, the stabilizing interactions with α-GTP are lost, which results in the flipping of GTP in the active site (Fig. S5, A–C). As a result, some of the native tubulin dimer interactions are lost (Fig. S5, A, B, D, and E). Determining the effects on the intradimer interface contacts, we demonstrated an alteration of the native contacts for the S140G mutant (Fig. S5, D and E), and the total number of intradimer interactions was also increased. This could lead to an increase in the overall stability of the mutant tubulin dimer, thus reducing its curvature. Indeed, further detailed analysis of the intradimer interface contacts (Sobolev et al., 1999) revealed that the S140G mutant forms an additional buried salt-bridge triad between α:N98 and β:R251, as well as β:R162 (Fig. 8, C–E). The strength of this salt–bridge interaction increases the stability and proximity in this region (Fig. S5, F and G), indicating that the S140G mutation leads to closer and stronger intradimer interface interactions.

Then, we compared the structures of Tuba1a and Tuba8. Superposing the models of these α-tubulins showed only slight changes in the core structure (Fig. 8 F). Next, we characterized the distribution of charges in the tubulin models by electrostatic

analyses. We found unique charge differences between Tuba1a and Tuba8 (Fig. 8 G) in the H1-S2 loop, which is known to interact laterally with M-loop of the tubulin molecule in the adjacent protofilament (Sui and Downing, 2010). Whereas in Tuba1a the electrostatic distribution in the H1-S2 loop complements well with the M loop region because of its positive-charge distribution, in Tuba8 this region shows negative-charge distribution (Fig. 8 G). These electrostatic differences might result in different binding affinities of Tuba1a and Tuba8 within the MT lattice and thus provide the structural basis for the functional specificities observed in MT polymerization studies for Tuba1a and Tuba8.

Altogether, our detailed analyses demonstrate for the first time the different functional contributions of specific isoforms of α-tubulin in neuronal cells. In particular, our molecular analyses show that mutant Tuba1a affects MT polymerization straightness and heterodimer stability, and the strict regulation of these parameters is clearly important for correct saltatory neuronal migration.

Discussion

Defective neuronal migration in *Tuba1a*-mutant mice

To date, studies of *Tuba1a*-mutant mice focused on organizational defects in different brain structures such as subtle wave-like perturbations in the neocortex, a fractured pyramidal layer in the hippocampus, and abnormalities in the superior colliculus (Keays et al., 2007). These were attributed to defects in neuronal migration, considering the well-known functions of MTs in this process and the disorganized cortical lamination in human patients carrying *TUBA1A* mutations. However, little was known concerning molecular and cellular mechanisms affected by the expression of mutated *TUBA1A*. In light of potential functional redundancy between different α-tubulin isotypes, it is intriguing that single heterozygous mutations can have a significant effect on MT functions. According to expression databases (e.g., http://mouse.brain-map.org/), *Tuba1a*, *Tuba1b*, *Tuba3a*, and *Tuba3b* are expressed in the adult RMS, whereas *Tuba8* is expressed in a subpopulation of cells in the OB (Braun et al., 2010). These isotypes often only differ by a few amino acids, and little is known about their specific functions. Transgenic lines and in situ hybridization for *Tuba1a* have demonstrated that most neuronal-committed postmitotic precursors along the RMS and in the OB are Tuba1a⁺ (and Sox2⁻) from P0 to the adult stage. (Miller et al., 1987; Coksaygan et al., 2006). Consistent with developmental studies showing that Tuba1a is expressed in β3-tubulin– and MAP-2–positive neurons (Gloster et al., 1994, 1999), it hence appears that this protein is expressed in most early postmitotic neurons with no exception in the RMS/OB system (Coksaygan et al., 2006).

Our current study confirms and adds to a previous study (Keays et al., 2007) that, despite the presence of different α-tubulin proteins, a heterozygote Tuba1a missense mutation in the mouse leads to a robust neuronal migratory defect. We also found that Tuba8 overexpression in vitro was able to counteract the effect of the Tuba1a S140G mutation. Hence, phenotypes would be expected to be different in coexpressing cells; however, this protein is not expressed in RMS migrating neurons (Braun et al., 2010). Recent data also show that the *Tuba8*-knockout mouse model presents no obvious defect in brain development but instead affected spermatogenesis (Diggle et al., 2017). Specific molecular features may be expected for these two proteins, which we confirmed here by structural modeling.

It still remains unclear whether the Tuba1a mutant represents a cell-autonomous consequence of Tuba1a S140G in neurons or whether non–cell autonomous defects are also involved. The dispersed glial phenotype observed in the adult RMS could either contribute to the neuronal defects or be a consequence of neuronal accumulation in the RMS. Previous expression data have shown that Tuba1a is restricted to neuronally committed cells and not expressed in glial cells (Gloster et al., 1999; Sawamoto et al., 2001; Coksaygan et al., 2006). Nevertheless, adult mutant mice present glial defects in regions where neurons do not accumulate abnormally (i.e., RMS1; Fig. S2, E–K). The reasons for this are currently unclear, although glial directionality signaling cues such as Slit/Robo may be abnormal (Kaneko et al., 2010), or defects in the overlying corpus callosum and/or oligodendrocyte progenitor migration defects might also contribute to glial abnormalities. Further studies are needed to understand whether Tuba1a influences MT regulation in glial cells directly or whether these are influenced by surrounding cells.

Diverse cellular functions and molecular mechanisms related to the Tuba1a S140G mutation

During neuronal migration, the extension of the leading process needs to be fine tuned, not only to provide directionality to the neurons, but also to constitute an anchor during the displacement of the soma (Solecki, 2012; Kawauchi, 2015). Biochemical studies have previously suggested that the S140G mutation leads to a reduction in the ability of the mutated tubulin to incorporate GTP, which is consistent with our modeling data. This may result in a declining efficiency of tubulin heterodimer formation (Keays et al., 2007) or affect the structure of the tubulin dimer as we show here and, consequently, the MT lattice. Changed MT dynamics in neuronal cells could be detrimental for the rapid construction and deconstruction of the leading process, as well as for its stabilization, affecting migration. Altered MT dynamics could also be the origin of increased neuronal branching observed in Tuba1a S140G-mutant neurons, a phenotype described previously for migrating INs with mutations of different MAPs such as p27[Kip1] or Dcx, which also affect dynamics by binding and stabilizing MTs (Kappeler et al., 2006; Koizumi et al., 2006; Belvindrah et al., 2011; Godin et al., 2012). Less stable MTs have been associated with membrane intrusion and emergence of new growth cones, the origins of neuronal processes. Excessive branching in mutant neurons appears in both fast and slow migrating populations and indistinctly in both soma and collaterals in unidirectional and non-unidirectional migrating neurons (unpublished data). It could be one of the major causes for the lack of directionality, as well as potentially contributing to N–C coupling defects to subsequently reroute the neurons from their main target, the OB.

Based on the availability of novel structural data for tubulin within the MT lattice (Alushin et al., 2014), we have modeled the impact of Tuba1a mutations into the structure of the α/β-tubulin dimer and demonstrated that the mutation straightens the natively curved (Nawrotek et al., 2011) dimer structure. This change in longitudinal curvature will potentially reduce the dynamics of the MT lattice, thus affecting architecture and function of the MT network. More stable dimers would also

translate into straighter polymerized MTs in cells, which is what we observed with live imaging in differentiated cells. It has also been shown recently that more flexible MTs generated by acetylation of lysine 40 of α-tubulin become more resistant to breakage (Portran et al., 2017; Xu et al., 2017). However, MT breakage by severing enzymes such as Spastin and Katanin is a prerequisite for neuronal branching (Yu et al., 2008). Thus, in the Tuba1a S140G-mutant condition, straighter MTs could be more susceptible to mechanical stress, breaking more often, and be at the origin of the excessive branching we observed.

The precise and dynamic regulation of N–C coupling is also a fundamental prerequisite for correct neuronal migration (Bellion et al., 2005; Higginbotham and Gleeson, 2007). Even subtle centrosomal dysfunction can cause massive IN migratory defects between the SVZ and OB (Endoh-Yamagami et al., 2010). Koizumi et al. (2006) also showed abnormal nuclear translocation in the *Dcx* mouse mutant. In the case of the Tuba1a S140G mutation, less curvature of the heterodimer and an increased MT straightness in the soma may contribute to an increased amplitude and augmented duration of N–C separation. Thus, less stable straighter MTs could affect the synchronization between nuclear and centrosome movements. Although migration for some specific neuronal subtypes and species might not require strict N–C coupling (Umeshima et al., 2007; Distel et al., 2010), our results for RMS neurons show that lack of adequate N–C oscillations contribute to their defective movement, characterized by increased pauses and slowed saltatory movements (Tanaka et al., 2004; Bellion et al., 2005; Sakakibara et al., 2014).

Our data show direct consequences of the Tuba1a S140G mutation on MT straightness and polymerization, which are likely to account for pathological alterations of neuronal migration in the mouse brain. We cannot exclude that the observed phenotypes are not also partially related to secondary consequences of altered MT structure, such as defects in MT-based intracellular vesicle traffic. For instance, the Tuba1a mutation could have an effect on the turnover of receptors such as integrins, which are required to interact with the cellular environment (Belvindrah et al., 2007), or guidance molecules such as Robo/Slits, netrins/DCC (deleted in colorectal cancer), Prokineticin2, S1P1, or SDF1 (Wu et al., 1999; Murase and Horwitz, 2002; Nguyen-Ba-Charvet et al., 2004; Ng et al., 2005; Lysko et al., 2014; Alfonso et al., 2015). This could potentially explain regional effects in the RMS. A possible deleterious cumulative effect of the Tuba1a S140G-mutant protein depending on the age of the neuroblast is also not excluded. Moreover, radial migration in the OB might also be affected, although in our experiments we observed no obvious defects in these migrating INs. Future studies could also address these questions.

In summary, we have demonstrated how variations in an *α-tubulin* gene mutated in cortical malformations can lead to neuronal migration defects in mice. Notably, we identified diverse effects that are related to an underlying conformational defect of the tubulin dimer and which are likely to alter MT curvature, flexibility, and polymerization straightness. Also, we reveal for the first time that the tight regulation of MT flexibility might constitute a prerequisite for correct branching and N–C coupling during saltatory neuronal migration, affecting speed and directionality. This work hence provides important new insights into molecular mechanisms underlying observed cellular defects. Conceptually, our work reveals how variations that generate apparently subtle alterations on the structure of tubulin molecules can potentially alter complex MT behavior in neuronal cells, thus leading to severe pathological conditions.

Materials and methods

Animals

The Tuba1a S140G (*Jenna*)–mutant mouse line (provided by D. Keays, IMP, Vienna, Austria) has been described previously (Keays et al., 2007) and is present on the C3H background. In brief, this mouse line was originally identified from an *N-ethyl-N*-nitrosourea (ENU) behavioral screen based on a semidominant hyperactive locomotor phenotype. For electroporation studies, P0–P2 RjOrl:SWISS mouse pups were obtained from Janvier Labs. Animals were maintained in standard conditions (12-h light/dark cycle and ad libitum access to dry food and water). All the experimental procedures were accomplished according to the European Community Council Directives (86/609/EEC) and European Union General Guidelines. Procedures were reviewed by the French Ministère de l'Enseignement Supérieur et de la Recherche and approved by a local ethical committee (agreement MESR 00984.02). Gad67-GFP mice were obtained from K. Obata's laboratory (National Institute for Physiological Sciences, Okazaki, Japan; Tamamaki et al., 2003). Crosses were also performed with ubiquitous CAG-GFP reporter mice (provided by M. Okabe, Osaka University, Osaka, Japan; Okabe et al., 1997) for certain video microscopy experiments.

Histology and immunostaining

Adult mice were deeply anaesthetized with pentobarbital and intracardially perfused with a solution of 4% paraformaldehyde in PBS, pH 7.2. The brains were removed, postfixed overnight in the same fixative solution at 4°C, and then stored in PBS. For studies in mouse pups and embryos, animals were rapidly decapitated, and brains were fixed in 4% paraformaldehyde overnight at 4°C. Then, dissected brains were embedded in 3.5% agarose (Invitrogen) and 8% sucrose (Sigma-Aldrich). 70-µm sagittal sections were prepared using a vibratome (VT1000S; Leica), and Nissl staining was performed on sections mounted on Superfrost slides (Thermo Fisher). The sections were analyzed with a brightfield microscope (Provis; Olympus) using a charge-coupled device (CCD) camera (CoolSNAP CF; Photometrics) with 2× (NA = 0.08) and 4× (NA = 0.13) objectives. Minimum contrasts were adjusted using ImageJ software (National Institutes of Health). Immunostaining was performed on floating sections in 24-well plates. Sections were incubated with PBS supplemented with 10% bovine serum (Life Technologies) and 0.2% Triton X-100 (blocking buffer) for 1 h at RT and incubated overnight at 4°C with the following primary antibodies in blocking buffer: mouse IgM anti–PSA-NCAM (clone 2-2B; Eurobio Abcys), rabbit polyclonal anti-GFP (A11122; Life Technologies), chicken anti-GFP (AB16901; Millipore), rabbit polyclonal anti-GFAP (ZO334; Dako), and rabbit polyclonal anti-calretinin (7697; Swant). Sections were rinsed three times with PBS for 10 min and incubated at RT for 2 h with secondary antibodies coupled to Alexa Fluor 488 or Alexa Fluor 568 (Life Technologies). Nuclei were counterstained for 10 min at RT with 1 µg/ml DAPI dihydrochloride (Sigma-Aldrich). Sections were rinsed with PBS and mounted with Fluoromount antifade mounting medium (Sigma-Aldrich). Stained sections were analyzed with epifluorescence (DM6000; Leica) with the following objectives: 4× (NA = 0.1), 10× (NA = 0.3), 20× (NA = 0.7), and 40× (NA = 1.25) linked with a CoolSNAP EZ CCD camera (Photometrics) controlled by Metamorph software (Molecular Devices) or a confocal microscope (SP5; Leica) with a 40× (NA = 1.25–0.75) objective controlled by LAS-AF software (Leica). Minimum contrast adjustment was performed using ImageJ software.

For Nissl staining experiments, three to seven littermate animals per condition and per stage were studied from E16.5, P0, P8, P21, and adult. RMS thickness and OB and GCL surfaces were quantified from three sections per adult animal (five animals per condition). All values are given as mean ± SEM, and a Student's *t* test was performed.

For calretinin staining quantification in the RMS, five control and four Tuba1a S140G-mutant littermate animals were studied; four rostrocaudal levels were selected along the RMS, and three adjacent slices per level were analyzed. The RMS was manually delineated with DAPI counterstaining. Automated countings were performed in four RMS regions with ICY Bioimage Analysis software using the Spot Detector plugin. All values are given as the mean of the number of calretinin+ cells per RMS ± SEM, and a Mann-Whitney test was performed.

For GFAP quantification in the RMS, four control and three Tuba1a S140G-mutant littermate adult animals were studied; three rostrocaudal levels were selected along the RMS (RMS1, RMS2, and RMS3), and three adjacent slices per level were analyzed. The GFAP+ staining from each region within a region of interest (ROI; 75.8 × 75.8 × 21 µm) was converted to a 3D volume using the Surface module from Imaris software (Bitplane). All values are given as the mean of GFAP+ glial fiber volume in cubic micrometers per ROI ± SEM, and a two-way ANOVA test was performed followed by Bonferroni posthoc tests.

For embryonic studies on GFP-positive brains, 20-µm serial coronal cryostat sections were prepared from frozen embryonic brains. Nine rostrocaudal levels were chosen for GFP analyses covering the lateral GE, medial GE, and caudal GE regions. Sections were imaged using a microscope (DM6000; Leica) with the following objectives: 4× (NA = 0.10) and 10× (NA = 0.3) linked to a CCD camera (CoolSNAP EZ; Photometrics) controlled by Metamorph software. For E13.5 migration distances, the region of the cortex studied was identified by drawing a horizontal line across the top of the GE. The reference distance was a line extended from this position to the apex of the cortex. The length of the GFP-positive migratory stream was then measured from the GE to the point where no further migrating neurons could be observed. The migration index was calculated from the ratio of this measurement to the reference distance. Coronal sections of E15.5 cortices were analyzed in the region of the developing hippocampus. Gad67-GFP–positive cells in marginal zone, intermediate zone, SVZ, and ventricular zone migratory streams were observed, and individual cells were counted in a defined ROI (ROI = 300 × 300 µm).

Electroporation procedures

P0–P2 RjOrl:SWISS mouse pups were anaesthetized on ice for 3 min before being maintained on a 4°C pad during the injection procedure. Mice were injected with the different plasmids directly into the lateral ventricle by transluminescence with an optical fiber (Leica). Approximately 2 µl of plasmid solutions at a concentration of 1 µg/µl (in endotoxin-free Tris-EDTA buffer; Qiagen) was injected with a 3.5-in glass-pulled pipette (Drummond) connected to a 15-µl Hamilton syringe. The brain was placed between a 10-mm Tweezertrode (Harvard Apparatus), with the positive pole oriented toward the injected side. Five, 50-ms square-wave pulses of 100 V, with a latency of 950 ms, were given with an electroporator (BTX ECM 830; Harvard Apparatus). Reanimated mice were kept warm on a 37°C heated pad and quickly returned to their mother after the procedure. Electroporated plasmids were as follows: Dcx-ires (internal ribosomal entry site)-GFP (Belvindrah et al., 2011); Dcx-Tuba1a S140G-ires-GFP obtained by subcloning Tuba1a S140G–pET23 (gift from G. Tian, New York University, New York, NY) into the Dcx-ires-GFP vector; Dcx–WT Tuba1a–ires-GFP for control conditions, produced by PCR mutagenesis from Dcx–Tuba1a S140G–ires-GFP; Dcx-Tuba8-ires-GFP obtained after amplification of Tuba8 by PCR from adult mouse brain cDNA

using the following primers: 5′-AATTCACTAGATGCATCACCATGA GGGAATGCATATCGGTC-3′ and 5′-GGAGAGGGGCGGATCCTT AAAATTCCTCCCCCTCATTCTC-3′ (the 1.35-kb PCR product was purified and cloned into pDcx-ires-GFP); and the pCAG-PACT-mKO1 vector (PACT domain of Pericentrin protein fused with the fluorescent protein mKO1), a gift from F. Matsuzaki (RIKEN CDB, Kobe, Japan) to track the centrosome.

For GFP staining quantification in the OB, four P1 mouse pups electroporated with the GFP construct only, five P1 with the Tuba1a control construct, and five P1 with the Tuba1a S140G-mutant construct were studied; two sections per mouse were selected for all three conditions. The SVZ, RMS, and OB were manually delineated with DAPI counterstaining. The total number of GFP+ cells in the three regions (SVZ, RMS, and OB) was quantified to avoid cell density variability within each region. This unbiased automatic counting was performed with ICY Bioimage Analysis software using the Spot Detector plugin. All values are given as a mean of percentage of GFP+ cells per region ± SEM, and a two-way ANOVA test was performed followed by Bonferroni posthoc tests.

Time-lapse video microscopy and analysis

For neuron migration analysis, 5 dpe, mouse pups were rapidly decapitated, and the brain was extracted. 150-µm sagittal brain slices were prepared with a vibratome (VT1000S; Leica) in cold HBSS (Life Technologies). Organotypic brain slices were mounted on a CM translucent membrane (Millipore) within a glass-bottom dish (Matek). Slices were perfused with the following culture medium: 46% MEM and 25% HBSS, supplemented with 25% horse serum, 2% 1 M Hepes, 6 mg/ml D-glucose, and primocin antibiotic (InVivoGen). The culture dish was placed within a thermostatic chamber maintained at 37°C. Time-lapse imaging was performed using an inverted confocal spinning-disk microscope (DMI4000; Leica) linked with a CCD camera (QuantEM:512c; Photometrics) controlled by Metamorph software. Typically, the slices were imaged from 12–24 h with a 20× (NA = 0.4) long-distance objective (Leica), and images were captured every 5 min; each frame in the time-lapse videos was generated from a 20 µm–thick z stack containing three separate images that were compressed into a single frame.

For neuronal speed quantification, 140 neurons in both conditions were studied by measuring instantaneous speeds manually with Metamorph software independent of direction. All values are given as mean ± SEM, and a Student's *t* test was performed. To distinguish slow and fast migration, we first performed a Hartigan's dip test, confirming that the frequency distribution of migration speeds was not unimodal. Then, using the AIC, we showed that the best fitting model for the frequency distribution is bimodal (AIC = 1,376.8 for a bimodal distribution). The threshold between low- and high-speed migration was defined mathematically as the intersection of the two Gaussian distributions fitting the frequency distributions of instantaneous speeds. Migration was correlated with the number of processes exhibited by the neuron. Instantaneous speeds, grouped according to fast (>75.48 µm/h) and slow (<75.48 µm/h) migration, were classified according to the four categories of morphology (Fig. 5 D): category 1, one process; category 2, two processes; category 3, three processes; and category 4, four processes. A total of 90 neurons were studied for each condition from three independent experiments. All values are given as a percentage of slow and fast migrating neurons ± SEM represented in these four categories for both control and Tuba1a S140G-mutant constructs. A two-way ANOVA test was performed followed by Bonferroni posthoc tests.

GE explant cultures were performed as previously described (Bellion et al., 2005; Kappeler et al., 2006). Time-lapse imaging was performed using an inverted confocal spinning-disk microscope

(DMI4000) linked with a CCD camera (QuantEM:512c) controlled by Metamorph software for 24 h with a 20× long distance objective (Leica), and images were captured every 5 min. Neuronal speed quantifications were performed by automated tracking of cell bodies using the Imaris image analysis software. A Mann-Whitney test was used to compare WT and mutant means.

For RMS migratory directionality quantification, each cell was plotted according to the angle formed between the beginning and end of the migratory sequence (from 0 to 360° with ranges of 30° and 0°/360° corresponding to dorsal, 90° to caudal, 180° to ventral, and 270° to rostral). A total of 90 neurons were studied for each condition from three independent experiments. All values are given as a percentage represented as a polar graph, and a χ^2 test was performed.

For morphology directionality–related quantifications, we manually correlated each migratory step with the number of processes exhibited by the neuron and the type of migration (unidirectional, i.e., parallel to the main migratory stream, or non-unidirectional migration, i.e., not parallel to the RMS and perpendicular to the stream or reversing and switching direction) according to the four categories of morphology described in the first paragraph of this section. A total of 100 neurons were studied for each condition from three independent experiments. All values are given as a percentage of unidirectional or non-unidirectional migrating neurons ± SEM represented in these four categories for both control and Tuba1a S140G-mutant constructs. A two-way ANOVA test was performed followed by Bonferroni posthoc tests.

For N–C coupling quantification, we measured every 5 min (time separating two acquisitions) the distance that separated the front part of the nucleus (GFP+ soma used as the limit for delineating the nucleus) from the centrosome (stained with PACT-mKO1). Over time, these distances vary and can be represented as oscillations, as at the beginning of the saltatory cycle, the distance is minimal but becomes maximal when the centrosome moves forward in the leading process and then becomes minimal again when the nucleus rejoins the centrosome. Oscillations were studied using an automated analysis of cycles in Matlab. In brief, the variation of distance (Δd) between the centrosome and nucleus was computed for each time and categorized between increasing (Δd > 3 µm), unchanged (−3 µm < Δd < 3 µm), and decreasing (Δd < −3 µm) distance. A cycle was determined as a succession of increasing and decreasing distances. Cycles could be interrupted by periods of unchanged distance as long as these were consecutive. For each cycle, its duration and its amplitude (maximum distance to minimum distance) were subsequently retrieved. A total of 93 neurons were studied for the control condition and 79 neurons for the S140G-mutant condition from three independent experiments. All values are given as mean ± SEM, and a Student's *t* test was performed.

To quantify the specific movement of the centrosome according to the migratory steps, we manually correlated all the cases when the nucleus joined the centrosome (= forward population) or on the contrary when the centrosome moved back to rejoin the nucleus (= backward population). A total of 30 neurons (94 cycles) were studied for the control condition and 40 neurons (158 cycles) for the Tuba1a S140G-mutant condition from three independent experiments. All values are given as a percentage of neurons in these two classes (forward or backward) in both conditions, and a Fisher test was used.

MT dynamic live imaging

To image the polymerization dynamics of MTs, we cultivated Neuro-2a cell lines (ATTC) with DMEM + 10% FCS (Life Technologies) directly on glass-bottom dishes (Ibidi Biosciences). 2 d before transfection, cells were cultivated in the same medium but deprived of serum to differentiate the cells (Evangelopoulos et al., 2005). Differentiated cells were recognized by the growth of processes. Then, cells were transfected with a normalized amount of total plasmids (3 µg) of Dcx–WT Tuba1a–ires-GFP, Dcx–Tuba1a S140G–ires-GFP, or Dcx–WT Tuba8–ires-GFP or Dcx–Tuba1a S140G–ires-GFP and Tuba8-ires-GFP together with EB3-mCherry vector (a gift from A. Andrieux, Institut des Neurosciences, Grenoble, France) using ExGen500 reagent (Euromedex) according to the manufacturer's recommendation. 24 h later, EB3-mCherry time-lapse imaging was performed using an inverted confocal spinning-disk microscope (DMI4000) with a 63× objective (NA = 1.4) linked with a CCD camera (QuantEM:512c;) controlled by Metamorph software for 4 min, and each frame in the time-lapse video was generated from a 0.6 µm–thick z stack containing three separate images taken every second that were compressed into a single frame.

For the MT polymerization quantification, the Track module from Imaris software was used to detect automatically the EB3-mCherry+ spots and track them over time. Different parameters were extracted, such as the speed of EB3-mCherry spots (by measuring the instantaneous speed of the spot) and the straightness of the EB3-mCherry polymerization (which is the total displacement of the spot divided by the length of the trajectory). For the studies in the soma, a total of 8,253 spots were tracked for the control condition, 8,933 spots for the Tuba1a S140G-mutant condition, 8,450 spots for the Tuba8 condition, and 9,182 spots for the Tuba1a S140G + Tuba8 condition. For the studies in the processes, a total of 2,185 spots were tracked for the control condition, 1,450 spots for the Tuba1a S140G-mutant condition, 2,242 spots for the Tuba8 condition, and 3,065 spots for the Tuba1a S140G + Tuba8 condition. All the quantifications were performed from three independent transfection experiments. For both the polymerization speed and the polymerization straightness, all values are given as mean ± SEM in the two cellular compartments (soma and processes), and a one-way ANOVA test was performed followed by Bonferroni posthoc tests.

Molecular dynamic simulations of WT and the S140G mutant

The atomic coordinates for the WT tubulin dimer were obtained from the crystal structure of tubulin in the Protein Data Bank (accession no. 3RYF; Nawrotek et al., 2011). The coordinates for missing residues in α-tubulin (42–44) were constructed using the Pymol software package (Schrödinger). The hydrogens for heavy atoms were added by the leap program in the AmberTools13 package (Case et al., 2005). Added hydrogens were energy minimized for 2,000 steps using the steepest descent algorithm. The partial atomic charges for GTP were obtained via quantum electronic structure calculations using the Gaussian 09 program (Gaussian Inc.) with the 6–31+G* basis set with the Hartree-Fock geometry optimization procedure. The atom-centered restrained electrostatic potential charges were determined by fitting the electrostatic potentials obtained from the calculated wave functions. The missing interaction parameters in the nucleotide were generated using the antechamber module in AmberTools.

After relaxing the added atoms in the gas phase, the structure was solvated in a cubic periodic box of explicit 3-site TIP3P water molecules extending 12 Å outside the protein on all sides. The system was neutralized, and 150 mM KCl was used to maintain the ionic strength. Particle-Mesh Ewald sum (Phillips et al., 2005) with a 10-Å cutoff was used to treat the long-range electrostatics. The SHAKE algorithm was used to constrain the bond lengths between heavy atoms and hydrogens (Ryckaert et al., 1977). Then, the system was equilibrated for 10 ns in the NPT ensemble with a simulation time step of 2 fs and further simulated to generate 25-ns trajectory data for WT. In the equilibrated structure of the WT tubulin dimer, the S140G mutation was introduced in the α-tubulin, and the mutant tubulin was further equilibrated for 10 ns following the same procedure as described for WT. Subsequently, a simulation run of 25 ns was generated for the

S140G-mutant protein. Both WT and mutant simulations were performed using the NAMD 2.10 package (Phillips et al., 2005) with an AMBERFF99SB force field (Hornak et al., 2006). The data were saved at an interval of 2 ps for analyses.

RMSD and RMSF analysis

To compare the overall structural variations during WT and mutant simulations, RMSD for the backbone atoms for WT and mutant were calculated. RMSD values were calculated for each frame along the entire trajectory as a function of time with respect to the respective starting structure of the WT and mutant simulation. The Cα RMSF was calculated to detect the mean fluctuations of each residue during simulations. RMSF calculates the movement of each Cα around its mean position, indicating highly flexible regions with larger RMSF values and rigid regions with lower RMSF values.

Intradimer bending angle analysis

To characterize the conformational flexibility of the tubulin dimer in WT and mutant simulations, the intradimer angle subtended by the axes of α-core helix H7 and β-core helix H7 was calculated along the respective trajectories. The vector drawn along the α:H7 was termed as $\hat{A}$, and the vector drawn along β:H7 was termed as $\hat{B}$. The intersection of the two vectors represents the intradimer bending angle of the tubulin dimer. We selected this angle because a relative translational motion was noted between α:H7 and β:H7 during simulations. The intradimer bending angle in the tubulin dimer was computed as $\Theta = \cos^{-1}\hat{A}.\hat{B}/|\hat{A}||\hat{B}|$.

Molecular modeling of Tuba1a and Tuba8

The amino acid sequences of Tuba1a and Tuba8 were retrieved from the UniProtKB database (accession nos. Q71U36 [Tuba1a] and Q9NY65 [Tuba8]). The structures of Tuba1a and Tuba8 were homology modeled using the I-TASSER server (Zhang, 2008; Roy et al., 2010) using the crystal structure of α-tubulin from Protein Data Bank accession no. 4I4T chain A as a template (Prota et al., 2013). The structural superposition and structure-based sequence alignment were performed using University of California, San Francisco chimera software (Pettersen et al., 2004).

Electrostatic analysis

The electrostatic analysis of Tuba1a and Tuba8 was calculated using the Poisson-Boltzmann equation implemented in the ABPS program (Baker et al., 2001). The structures were assigned the correct protonation state of residues using PROPKA, and the PQR files were generated using the PDB2PQR server (Dolinsky et al., 2004). Electrostatic calculations were performed using the following parameters: ionic strength of 150 mM, ionic radius 1.5 Å, dielectric constant for the protein interior 1, and dielectric constant in water 80.

Online supplemental material

Fig. S1 shows cortical IN migratory defects in *Tuba1a*-mutant mice during embryonic development. Fig. S2 shows GFAP staining in postnatal and adult mutant mice or after electroporation of the Tuba1a-S140G construct. Fig. S3 describes developmental studies of the RMS in *Tuba1a*-mutant mice. Figs. S4 and S5 describe dynamic simulations of Tuba1a versus Tuba1a S140G and structural consequences of the mutation with GTP and intradimer interface interactions, respectively. Videos 1 and 2 show time-lapse images of GFP+ neurons in organotypic slices from Tuba1a-GFP– and Tuba1a-S140G-GFP–electroporated mice, respectively. Videos 3 and 4 show time-lapse images of GFP+ neurons in organotypic slices from Tuba1a-GFP (green)/PACT-mKO (orange) and Tuba1a-S140G-GFP(green)–/PACT-mKO (orange)–

electroporated mice, respectively. Videos 5–8 show an example of N2a differentiated cells cotransfected with EB3-mCherry (red) and Tuba1a-GFP, Tuba1a-S140G-GFP, Tuba8-GFP, or Tuba1a-S140G-GFP and Tuba8 constructs, respectively. Table S1 describes MT polymerization dynamic studies after expression of Tuba1a, Tuba1a S140G-mutant, Tuba8, and Tuba1a S140G + Tuba8 constructs. Supplementary Matlab code is available as a text file and contains the script that determines the N–C distance during saltatory movements by detecting the start/stop of each cycle and retrieving both their amplitude and duration. If necessary, it also performs comparisons between two populations (e.g., WT and mutants).

and F. Francis conceived the experiments, analyzed the data, and wrote the manuscript.

References

Abdollahi, M.R., E. Morrison, T. Sirey, Z. Molnar, B.E. Hayward, I.M. Carr, K. Springell, C.G. Woods, M. Ahmed, L. Hattingh, et al. 2009. Mutation of the variant α-tubulin TUBA8 results in polymicrogyria with optic nerve hypoplasia. *Am. J. Hum. Genet.* 85:737–744. http://dx.doi.org/10.1016/j.ajhg.2009.10.007

Alfonso, J., H. Penkert, C. Duman, A. Zuccotti, and H. Monyer. 2015. Downregulation of sphingosine 1-phosphate receptor 1 promotes the switch from tangential to radial migration in the OB. *J. Neurosci.* 35:13659–13672. http://dx.doi.org/10.1523/JNEUROSCI.1353-15.2015

Alushin, G.M., G.C. Lander, E.H. Kellogg, R. Zhang, D. Baker, and E. Nogales. 2014. High-resolution microtubule structures reveal the structural transitions in αβ-tubulin upon GTP hydrolysis. *Cell.* 157:1117–1129. http://dx.doi.org/10.1016/j.cell.2014.03.053

Bahi-Buisson, N., and M. Cavallin. 2016. Tubulinopathies Overview. *In* GeneReviews. R.A. Pagon, M.P. Adam, H.H. Ardinger, S.E. Wallace, A. Amemiya, L.J.H. Bean, T.D. Bird, N. Ledbetter, H.C. Mefford, R.J.H. Smith, and K. Stephens, editors. University of Washington, Seattle. Available at: https://www.ncbi.nlm.nih.gov/books/NBK350554/

Bahi-Buisson, N., K. Poirier, N. Boddaert, Y. Saillour, L. Castelnau, N. Philip, G. Buyse, L. Villard, S. Joriot, S. Marret, et al. 2008. Refinement of cortical dysgeneses spectrum associated with TUBA1A mutations. *J. Med. Genet.* 45:647–653. http://dx.doi.org/10.1136/jmg.2008.058073

Bahi-Buisson, N., K. Poirier, F. Fourniol, Y. Saillour, S. Valence, N. Lebrun, M. Hully, C.F. Bianco, N. Boddaert, C. Elie, et al. LIS-Tubulinopathies Consortium. 2014. The wide spectrum of tubulinopathies: what are the key features for the diagnosis? *Brain.* 137:1676–1700. http://dx.doi.org/10.1093/brain/awu082

Baker, N.A., D. Sept, S. Joseph, M.J. Holst, and J.A. McCammon. 2001. Electrostatics of nanosystems: application to microtubules and the ribosome. *Proc. Natl. Acad. Sci. USA.* 98:10037–10041. http://dx.doi.org/10.1073/pnas.181342398

Bellion, A., J.P. Baudoin, C. Alvarez, M. Bornens, and C. Métin. 2005. Nucleokinesis in tangentially migrating neurons comprises two alternating phases: forward migration of the Golgi/centrosome associated with centrosome splitting and myosin contraction at the rear. *J. Neurosci.* 25:5691–5699. http://dx.doi.org/10.1523/JNEUROSCI.1030-05.2005

Belvindrah, R., S. Hankel, J. Walker, B.L. Patton, and U. Müller. 2007. β1 integrins control the formation of cell chains in the adult rostral migratory stream. *J. Neurosci.* 27:2704–2717. http://dx.doi.org/10.1523/JNEUROSCI.2991-06.2007

Belvindrah, R., F. Lazarini, and P.-M. Lledo. 2009. Postnatal neurogenesis: from neuroblast migration to integration into mature circuits. *Rev. Neurosci.* 20:331–346. http://dx.doi.org/10.1515/REVNEURO.2009.20.5-6.331

Belvindrah, R., A. Nissant, and P.M. Lledo. 2011. Abnormal neuronal migration changes the fate of developing neurons in the postnatal olfactory bulb. *J. Neurosci.* 31:7551–7562. http://dx.doi.org/10.1523/JNEUROSCI.6716-10.2011

Bozoyan, L., J. Khlghatyan, and A. Saghatelyan. 2012. Astrocytes control the development of the migration-promoting vasculature scaffold in the postnatal brain via VEGF signaling. *J. Neurosci.* 32:1687–1704. http://dx.doi.org/10.1523/JNEUROSCI.5531-11.2012

Braun, A., M. Breuss, M.C. Salzer, J. Flint, N.J. Cowan, and D.A. Keays. 2010. Tuba8 is expressed at low levels in the developing mouse and human brain. *Am. J. Hum. Genet.* 86:819–822. http://dx.doi.org/10.1016/j.ajhg.2010.03.019

Case, D.A., T.E. Cheatham III, T. Darden, H. Gohlke, R. Luo, K.M. Merz Jr., A. Onufriev, C. Simmerling, B. Wang, and R.J. Woods. 2005. The Amber biomolecular simulation programs. *J. Comput. Chem.* 26:1668–1688. http://dx.doi.org/10.1002/jcc.20290

Chakraborti, S., K. Natarajan, J. Curiel, C. Janke, and J. Liu. 2016. The emerging role of the tubulin code: From the tubulin molecule to neuronal function and disease. *Cytoskeleton (Hoboken).* 73:521–550. http://dx.doi.org/10.1002/cm.21290

Chazal, G., P. Durbec, A. Jankovski, G. Rougon, and H. Cremer. 2000. Consequences of neural cell adhesion molecule deficiency on cell mi-gration in the rostral migratory stream of the mouse. *J. Neurosci.* 20:1446–1457.

Coksaygan, T., T. Magnus, J. Cai, M. Mughal, A. Lepore, H. Xue, I. Fischer, and M.S. Rao. 2006. Neurogenesis in Tα-1 tubulin transgenic mice during development and after injury. *Exp. Neurol.* 197:475–485. http://dx.doi.org/10.1016/j.expneurol.2005.10.030

Corbin, J.G., S. Nery, and G. Fishell. 2001. Telencephalic cells take a tangent: non-radial migration in the mammalian forebrain. *Nat. Neurosci.* 4:1177–1182. http://dx.doi.org/10.1038/nn749

Diggle, C.P., I. Martinez-Garay, Z. Molnar, M.H. Brinkworth, E. White, E. Fowler, R. Hughes, B.E. Hayward, I.M. Carr, C.M. Watson, et al. 2017. A tubulin alpha 8 mouse knockout model indicates a likely role in spermatogenesis but not in brain development. *PLoS One.* 12:e0174264. http://dx.doi.org/10.1371/journal.pone.0174264

Distel, M., J.C. Hocking, K. Volkmann, and R.W. Köster. 2010. The centrosome neither persistently leads migration nor determines the site of axonogenesis in migrating neurons in vivo. *J. Cell Biol.* 191:875–890. http://dx.doi.org/10.1083/jcb.201004154

Doetsch, F., and A. Alvarez-Buylla. 1996. Network of tangential pathways for neuronal migration in adult mammalian brain. *Proc. Natl. Acad. Sci. USA.* 93:14895–14900. http://dx.doi.org/10.1073/pnas.93.25.14895

Dolinsky, T.J., J.E. Nielsen, J.A. McCammon, and N.A. Baker. 2004. PDB2PQR: an automated pipeline for the setup of Poisson-Boltzmann electrostatics calculations. *Nucleic Acids Res.* 32:W665–W667. http://dx.doi.org/10.1093/nar/gkh381

Endoh-Yamagami, S., K.M. Karkar, S.R. May, I. Cobos, M.T. Thwin, J.E. Long, A.M. Ashique, K. Zarbalis, J.L. Rubenstein, and A.S. Peterson. 2010. A mutation in the pericentrin gene causes abnormal interneuron migration to the olfactory bulb in mice. *Dev. Biol.* 340:41–53. http://dx.doi.org/10.1016/j.ydbio.2010.01.017

Evangelopoulos, M.E., J. Weis, and A. Krüttgen. 2005. Signalling pathways leading to neuroblastoma differentiation after serum withdrawal: HDL blocks neuroblastoma differentiation by inhibition of EGFR. *Oncogene.* 24:3309–3318. http://dx.doi.org/10.1038/sj.onc.1208494

Fallet-Bianco, C., L. Loeuillet, K. Poirier, P. Loget, F. Chapon, L. Pasquier, Y. Saillour, C. Beldjord, J. Chelly, and F. Francis. 2008. Neuropathological phenotype of a distinct form of lissencephaly associated with mutations in TUBA1A. *Brain.* 131:2304–2320. http://dx.doi.org/10.1093/brain/awn155

Fallet-Bianco, C., A. Laquerrière, K. Poirier, F. Razavi, F. Guimiot, P. Dias, L. Loeuillet, K. Lascelles, C. Beldjord, N. Carion, et al. 2014. Mutations in tubulin genes are frequent causes of various foetal malformations of cortical development including microlissencephaly. *Acta Neuropathol. Commun.* 2:69. http://dx.doi.org/10.1186/2051-5960-2-69

Gheusi, G., G. Lepousez, and P.M. Lledo. 2012. Adult-born neurons in the olfactory bulb: integration and functional consequences. *Curr. Top. Behav. Neurosci.* 15:49–72. http://dx.doi.org/10.1007/7854_2012_228

Gloster, A., W. Wu, A. Speelman, S. Weiss, C. Causing, C. Pozniak, B. Reynolds, E. Chang, J.G. Toma, and F.D. Miller. 1994. The T alpha 1 alpha-tubulin promoter specifies gene expression as a function of neuronal growth and regeneration in transgenic mice. *J. Neurosci.* 14:7319–7330.

Gloster, A., H. El-Bizri, S.X. Bamji, D. Rogers, and F.D. Miller. 1999. Early induction of Tα1 α-tubulin transcription in neurons of the developing nervous system. *J. Comp. Neurol.* 405:45–60. http://dx.doi.org/10.1002/(SICI)1096-9861(19990301)405:1<45::AID-CNE4>3.0.CO;2-M

Godin, J.D., N. Thomas, S. Laguesse, L. Malinouskaya, P. Close, O. Malaise, A. Purnelle, O. Raineteau, K. Campbell, M. Fero, et al. 2012. p27(Kip1) is a microtubule-associated protein that promotes microtubule polymerization during neuron migration. *Dev. Cell.* 23:729–744. http://dx.doi.org/10.1016/j.devcel.2012.08.006

Hack, I., M. Bancila, K. Loulier, P. Carroll, and H. Cremer. 2002. Reelin is a detachment signal in tangential chain-migration during postnatal neurogenesis. *Nat. Neurosci.* 5:939–945. http://dx.doi.org/10.1038/nn923

Higginbotham, H.R., and J.G. Gleeson. 2007. The centrosome in neuronal development. *Trends Neurosci.* 30:276–283. http://dx.doi.org/10.1016/j.tins.2007.04.001

Hornak, V., R. Abel, A. Okur, B. Strockbine, A. Roitberg, and C. Simmerling. 2006. Comparison of multiple Amber force fields and development of improved protein backbone parameters. *Proteins.* 65:712–725. http://dx.doi.org/10.1002/prot.21123

Jaglin, X.H., and J. Chelly. 2009. Tubulin-related cortical dysgeneses: microtubule dysfunction underlying neuronal migration defects. *Trends Genet.* 25:555–566. http://dx.doi.org/10.1016/j.tig.2009.10.003

James, R., Y. Kim, P.E. Hockberger, and F.G. Szele. 2011. Subventricular zone cell migration: lessons from quantitative two-photon microscopy. *Front. Neurosci.* 5:30. http://dx.doi.org/10.3389/fnins.2011.00030

Jankovski, A., and C. Sotelo. 1996. Subventricular zone-olfactory bulb migratory pathway in the adult mouse: cellular composition and specificity as determined by heterochronic and heterotopic transplantation. *J. Comp. Neurol.* 371:376–396. http://dx.doi.org/10.1002/(SICI)1096 -9861(19960729)371:3<376::AID-CNE3>3.0.CO;2-#

Kaneko, N., O. Marín, M. Koike, Y. Hirota, Y. Uchiyama, J.Y. Wu, Q. Lu, M. Tessier-Lavigne, A. Alvarez-Buylla, H. Okano, et al. 2010. New neurons clear the path of astrocytic processes for their rapid migration in the adult brain. *Neuron.* 67:213–223. http://dx.doi.org/10.1016/j.neuron .2010.06.018

Kapitein, L.C., and C.C. Hoogenraad. 2015. Building the neuronal microtubule cytoskeleton. *Neuron.* 87:492–506. http://dx.doi.org/10.1016/j.neuron .2015.05.046

Kappeler, C., Y. Saillour, J.P. Baudoin, F.P. Tuy, C. Alvarez, C. Houbron, P. Gaspar, G. Hamard, J. Chelly, C. Métin, and F. Francis. 2006. Branching and nucleokinesis defects in migrating interneurons derived from doublecortin knockout mice. *Hum. Mol. Genet.* 15:1387–1400. http ://dx.doi.org/10.1093/hmg/ddl062

Kawauchi, T. 2015. Cellullar insights into cerebral cortical development: focusing on the locomotion mode of neuronal migration. *Front. Cell. Neurosci.* 9:394. http://dx.doi.org/10.3389/fncel.2015.00394

Keays, D.A., G. Tian, K. Poirier, G.J. Huang, C. Siebold, J. Cleak, P.L. Oliver, M. Fray, R.J. Harvey, Z. Molnár, et al. 2007. Mutations in α-tubulin cause abnormal neuronal migration in mice and lissencephaly in humans. *Cell.* 128:45–57. http://dx.doi.org/10.1016/j.cell.2006.12.017

Koizumi, H., H. Higginbotham, T. Poon, T. Tanaka, B.C. Brinkman, and J.G. Gleeson. 2006. Doublecortin maintains bipolar shape and nuclear translocation during migration in the adult forebrain. *Nat. Neurosci.* 9:779–786. http://dx.doi.org/10.1038/nn1704

Kumar, R.A., D.T. Pilz, T.D. Babatz, T.D. Cushion, K. Harvey, M. Topf, L. Yates, S. Robb, G. Uyanik, G.M. Mancini, et al. 2010. *TUBA1A* mutations cause wide spectrum lissencephaly (smooth brain) and suggest that multiple neuronal migration pathways converge on alpha tubulins. *Hum. Mol. Genet.* 19:2817–2827. http://dx.doi.org/10.1093/hmg/ddq182

Lalli, G. 2014. Extracellular signals controlling neuroblast migration in the postnatal brain. *Adv. Exp. Med. Biol.* 800:149–180. http://dx.doi.org/10 .1007/978-94-007-7687-6_9

Lledo, P.M., M. Alonso, and M.S. Grubb. 2006. Adult neurogenesis and functional plasticity in neuronal circuits. *Nat. Rev. Neurosci.* 7:179–193. http://dx.doi.org/10.1038/nrn1867

Lois, C., and A. Alvarez-Buylla. 1994. Long-distance neuronal migration in the adult mammalian brain. *Science.* 264:1145–1148. http://dx.doi.org/10 .1126/science.8178174

Luskin, M.B. 1993. Restricted proliferation and migration of postnatally generated neurons derived from the forebrain subventricular zone. *Neuron.* 11:173–189. http://dx.doi.org/10.1016/0896-6273(93)90281-U

Lysko, D.E., M. Putt, and J.A. Golden. 2014. SDF1 reduces interneuron leading process branching through dual regulation of actin and microtubules. *J. Neurosci.* 34:4941–4962. http://dx.doi.org/10.1523/JNEUROSCI.4351 -12.2014

Miller, F.D., C.C. Naus, M. Durand, F.E. Bloom, and R.J. Milner. 1987. Isotypes of alpha-tubulin are differentially regulated during neuronal maturation. *J. Cell Biol.* 105:3065–3073. http://dx.doi.org/10.1083/jcb.105.6.3065

Murase, S., and A.F. Horwitz. 2002. Deleted in colorectal carcinoma and differ- entially expressed integrins mediate the directional migration of neural precursors in the rostral migratory stream. *J. Neurosci.* 22:3568–3579.

Nawrotek, A., M. Knossow, and B. Gigant. 2011. The determinants that govern microtubule assembly from the atomic structure of GTP-tubulin. *J. Mol. Biol.* 412:35–42. http://dx.doi.org/10.1016/j.jmb.2011.07.029

Ng, K.L., J.D. Li, M.Y. Cheng, F.M. Leslie, A.G. Lee, and Q.Y. Zhou. 2005. Dependence of olfactory bulb neurogenesis on prokineticin 2 signaling. *Science.* 308:1923–1927. http://dx.doi.org/10.1126/science.1112103

Nguyen-Ba-Charvet, K.T., N. Picard-Riera, M. Tessier-Lavigne, A. Baron-Van Evercooren, C. Sotelo, and A. Chédotal. 2004. Multiple roles for slits in the control of cell migration in the rostral migratory stream. *J. Neurosci.* 24:1497–1506. http://dx.doi.org/10.1523/JNEUROSCI.4729-03.2004

Okabe, M., M. Ikawa, K. Kominami, T. Nakanishi, and Y. Nishimune. 1997. 'Green mice' as a source of ubiquitous green cells. *FEBS Lett.* 407:313– 319. http://dx.doi.org/10.1016/S0014-5793(97)00313-X

Pallotto, M., and F. Deprez. 2014. Regulation of adult neurogenesis by GABAergic transmission: signaling beyond GABAA-receptors. *Front. Cell. Neurosci.* 8:166. http://dx.doi.org/10.3389/fncel.2014.00166

Pencea, V., and M.B. Luskin. 2003. Prenatal development of the rodent rostral migratory stream. *J. Comp. Neurol.* 463:402–418. http://dx.doi.org/10 .1002/cne.10746

Pettersen, E.F., T.D. Goddard, C.C. Huang, G.S. Couch, D.M. Greenblatt, E.C. Meng, and T.E. Ferrin. 2004. UCSF Chimera—a visualization system for exploratory research and analysis. *J. Comput. Chem.* 25:1605– 1612. http://dx.doi.org/10.1002/jcc.20084

Phillips, J.C., R. Braun, W. Wang, J. Gumbart, E. Tajkhorshid, E. Villa, C. Chipot, R.D. Skeel, L. Kalé, and K. Schulten. 2005. Scalable molecular dynamics with NAMD. *J. Comput. Chem.* 26:1781–1802. http://dx.doi.org/10.1002 /jcc.20289

Poirier, K., D.A. Keays, F. Francis, Y. Saillour, N. Bahi, S. Manouvrier, C. Fallet-Bianco, L. Pasquier, A. Toutain, F.P. Tuy, et al. 2007. Large spectrum of lissencephaly and pachygyria phenotypes resulting from de novo missense mutations in tubulin alpha 1A (*TUBA1A*). *Hum. Mutat.* 28:1055–1064. http://dx.doi.org/10.1002/humu.20572

Poirier, K., Y. Saillour, F. Fourniol, F. Francis, I. Souville, S. Valence, I. Desguerre, J. Marie Lepage, N. Boddaert, M. Line Jacquemont, et al. 2013. Expanding the spectrum of *TUBA1A*-related cortical dysgenesis to Polymicrogyria. *Eur. J. Hum. Genet.* 21:381–385. http://dx.doi.org/10 .1038/ejhg.2012.195

Portran, D., L. Schaedel, Z. Xu, M. Théry, and M.V. Nachury. 2017. Tubulin acetylation protects long-lived microtubules against mechanical ageing. *Nat. Cell Biol.* 19:391–398. http://dx.doi.org/10.1038/ncb3481

Prota, A.E., K. Bargsten, D. Zurwerra, J.J. Field, J.F. Díaz, K.H. Altmann, and M.O. Steinmetz. 2013. Molecular mechanism of action of microtubule-stabilizing anticancer agents. *Science.* 339:587–590. http://dx.doi.org/10 .1126/science.1230582

Reiner, O., and T. Sapir. 2009. Polarity regulation in migrating neurons in the cortex. *Mol. Neurobiol.* 40:1–14. http://dx.doi.org/10.1007/s12035-009 -8065-0

Roy, A., A. Kucukural, and Y. Zhang. 2010. I-TASSER: a unified platform for automated protein structure and function prediction. *Nat. Protoc.* 5:725– 738. http://dx.doi.org/10.1038/nprot.2010.5

Ryckaert, J.-P., G. Ciccotti, and H.J.C. Berendsen. 1977. Numerical integration of the cartesian equations of motion of a system with constraints: molecular dynamics of *n*-alkanes. *J. Comput. Phys.* 23:327–341. http:// dx.doi.org/10.1016/0021-9991(77)90098-5

Sakakibara, A., T. Sato, R. Ando, N. Noguchi, M. Masaoka, and T. Miyata. 2014. Dynamics of centrosome translocation and microtubule organization in neocortical neurons during distinct modes of polarization. *Cereb. Cortex.* 24:1301–1310. http://dx.doi.org/10.1093/cercor/bhs411

Sawamoto, K., A. Yamamoto, A. Kawaguchi, M. Yamaguchi, K. Mori, S.A. Goldman, and H. Okano. 2001. Direct isolation of committed neuronal progenitor cells from transgenic mice coexpressing spectrally distinct fluorescent proteins regulated by stage-specific neural promoters. *J. Neurosci. Res.* 65:220–227. http://dx.doi.org/10.1002/jnr.1145

Sobolev, V., A. Sorokine, J. Prilusky, E.E. Abola, and M. Edelman. 1999. Automated analysis of interatomic contacts in proteins. *Bioinformatics.* 15:327–332. http://dx.doi.org/10.1093/bioinformatics/15.4.327

Solecki, D.J. 2012. Sticky situations: recent advances in control of cell adhesion during neuronal migration. *Curr. Opin. Neurobiol.* 22:791–798. http://dx .doi.org/10.1016/j.conb.2012.04.010

Sonego, M., M. Oberoi, J. Stoddart, S. Gajendra, R. Hendricusdottir, F. Oozeer, D.C. Worth, C. Hobbs, B.J. Eickholt, P.R. Gordon-Weeks, et al. 2015. Drebrin regulates neuroblast migration in the postnatal mammalian brain. *PLoS One.* 10:e0126478. http://dx.doi.org/10.1371/journal.pone .0126478

Sui, H., and K.H. Downing. 2010. Structural basis of interprotofilament interaction and lateral deformation of microtubules. *Structure.* 18:1022– 1031. http://dx.doi.org/10.1016/j.str.2010.05.010

Tamamaki, N., Y. Yanagawa, R. Tomioka, J. Miyazaki, K. Obata, and T. Kaneko. 2003. Green fluorescent protein expression and colocalization with calretinin, parvalbumin, and somatostatin in the GAD67-GFP knock-in mouse. *J. Comp. Neurol.* 467:60–79. http://dx.doi.org/10.1002/cne.10905

Tanaka, T., F.F. Serneo, C. Higgins, M.J. Gambello, A. Wynshaw-Boris, and J.G. Gleeson. 2004. Lis1 and doublecortin function with dynein to mediate coupling of the nucleus to the centrosome in neuronal migration. *J. Cell Biol.* 165:709–721. http://dx.doi.org/10.1083/jcb.200309025

Tischfield, M.A., and E.C. Engle. 2010. Distinct α- and β-tubulin isotypes are required for the positioning, differentiation and survival of neurons: new support for the 'multi-tubulin' hypothesis. *Biosci. Rep.* 30:319–330. http ://dx.doi.org/10.1042/BSR20100025

Umeshima, H., T. Hirano, and M. Kengaku. 2007. Microtubule-based nuclear movement occurs independently of centrosome positioning in migrating neurons. *Proc. Natl. Acad. Sci. USA.* 104:16182–16187. http://dx.doi.org /10.1073/pnas.0708047104

Whitman, M.C., W. Fan, L. Rela, D.J. Rodriguez-Gil, and C.A. Greer. 2009. Blood vessels form a migratory scaffold in the rostral migratory stream. *J. Comp. Neurol.* 516:94–104. http://dx.doi.org/10.1002/cne.22093

Wichterle, H., J.M. Garcia-Verdugo, and A. Alvarez-Buylla. 1997. Direct evidence for homotypic, glia-independent neuronal migration. *Neuron*. 18:779–791. http://dx.doi.org/10.1016/S0896-6273(00)80317-7

Wu, W., K. Wong, J. Chen, Z. Jiang, S. Dupuis, J.Y. Wu, and Y. Rao. 1999. Directional guidance of neuronal migration in the olfactory system by the protein Slit. *Nature*. 400:331–336. http://dx.doi.org/10.1038/22477

Xu, Z., L. Schaedel, D. Portran, A. Aguilar, J. Gaillard, M.P. Marinkovich, M. Théry, and M.V. Nachury. 2017. Microtubules acquire resistance from mechanical breakage through intralumenal acetylation. *Science*. 356:328–332. http://dx.doi.org/10.1126/science.aai8764

Yu, W., L. Qiang, J.M. Solowska, A. Karabay, S. Korulu, and P.W. Baas. 2008. The microtubule-severing proteins spastin and katanin participate differently in the formation of axonal branches. *Mol. Biol. Cell*. 19:1485–1498. http://dx.doi.org/10.1091/mbc.E07-09-0878

Zhang, Y. 2008. I-TASSER server for protein 3D structure prediction. *BMC Bioinformatics*. 9:40. http://dx.doi.org/10.1186/1471-2105-9-40